

This is an Open Access document downloaded from ORCA, Cardiff University's institutional repository: <https://orca.cardiff.ac.uk/id/eprint/112610/>

This is the author's version of a work that was submitted to / accepted for publication.

Citation for final published version:

Aubineau, Jérémie, El Albani, Abderrazak, Chi Fru, Ernest, Gingras, Murray, Batonneau, Yann, Buatois, Luis A., Geffroy, Claude, Labanowski, Jérôme, Laforest, Claude, Lemée, Laurent, Mángano, Maria G., Meunier, Alain, Pierson-Wickmann, Anne-Catherine, Recourt, Philippe, Riboulleau, Armelle, Trentesaux, Alain and Konhauser, Kurt O. 2018. Unusual microbial mat-related structural diversity 2.1 billion years ago and implications for the Francevillian biota. *Geobiology* 16 (5), pp. 476-497. 10.1111/gbi.12296

Publishers page: <http://dx.doi.org/10.1111/gbi.12296>

Please note:

Changes made as a result of publishing processes such as copy-editing, formatting and page numbers may not be reflected in this version. For the definitive version of this publication, please refer to the published source. You are advised to consult the publisher's version if you wish to cite this paper.

This version is being made available in accordance with publisher policies. See <http://orca.cf.ac.uk/policies.html> for usage policies. Copyright and moral rights for publications made available in ORCA are retained by the copyright holders.



# 1 Unusual microbial mat-related structural diversity 2.1 billion 2 years ago and implications for the Francevillian biota

3 Jérémie Aubineau<sup>1</sup>, Abderrazak El Albani<sup>1\*</sup>, Ernest Chi Fru<sup>2</sup>, Murray Gingras<sup>3</sup>, Yann  
4 Batonneau<sup>1</sup>, Luis A. Buatois<sup>4</sup>, Claude Geffroy<sup>1</sup>, Jérôme Labanowski<sup>1</sup>, Claude Laforest<sup>1</sup>,  
5 Laurent Lemée<sup>1</sup>, M. Gabriela Mángano<sup>4</sup>, Alain Meunier<sup>1</sup>, Anne-Catherine Pierson-  
6 Wickmann<sup>5</sup>, Philippe Recourt<sup>6</sup>, Armelle Riboulleau<sup>6</sup>, Alain Trentesaux<sup>6</sup> & Kurt Konhauser<sup>3</sup>

7  
8 <sup>1</sup>UMR CNRS IC2MP 7285, University of Poitiers, 86073 Poitiers, France. <sup>2</sup>Cardiff  
9 University, Main Building, Room 2.15B Park Place Cardiff, CF10 3AT, UK. <sup>3</sup>Department of  
10 Earth and Atmospheric Sciences University of Alberta Edmonton, Alberta, T6G 2E3 Canada.  
11 <sup>4</sup>Department of Geological Sciences, University of Saskatchewan, Saskatoon, SK S7N 5A5,  
12 Canada. <sup>5</sup>Department Geosciences, UMR 6118, University of Rennes 1, 35042 Rennes,  
13 France. <sup>6</sup>UMR 8187 LOG CNRS, University of Lille, ULCO, 59655, Villeneuve d'Ascq,  
14 France.

## 16 Abstract

17 The 2.1-billion-year-old (Ga) Francevillian series in Gabon hosts some of the oldest reported  
18 macroscopic fossils of various sizes and shapes, stimulating new debates on the origin,  
19 evolution and organization of early complex life. Here we document ten representative types  
20 of exceptionally well-preserved mat-related structures, comprising 'elephant-skin' textures,  
21 putative macro-tufted microbial mats, domal buildups, flat pyritized structures, discoidal  
22 microbial colonies, horizontal mat growth patterns, wrinkle structures, 'kinneyia' structures,  
23 linear patterns and nodule-like structures. A combination of petrographic analyses, scanning  
24 electron microscopy, Raman spectroscopy and organic elemental analyses of carbon-rich  
25 laminae and microtexture converge on a biological origin for these structures. The observed  
26 microtextures encompass oriented grains, floating silt-sized quartz grains, concentrated heavy

1  
2  
3 27 minerals, randomly oriented clays, wavy-crinkly laminae and pyritized structures. Based on  
4  
5 28 comparisons with modern analogues, as well as an average  $\delta^{13}\text{C}$  organic matter ( $C_{\text{org}}$ )  
6  
7 29 composition of  $-32.94 \pm 1.17\text{‰}$  (1 standard deviation, s.d.) with an outlier of  $-41.26\text{‰}$ , we  
8  
9 30 argue that the mat-related structures contain relicts of multiple carbon pathways including  
10  
11 31 heterotrophic recycling of photosynthetically derived  $C_{\text{org}}$ . Moreover, the relatively close  
12  
13 32 association of the macroscopic fossil assemblages to the microbial mats may imply that  
14  
15 33 microbial communities acted as potential benthic  $\text{O}_2$  oases linked to oxyphototrophic  
16  
17 34 cyanobacterial mats and grazing grounds. In addition, the mat's presence likely improved the  
18  
19 35 preservation of the oldest large colonial organisms, as they are known to strongly biostabilize  
20  
21 36 sediments. Our findings highlight the oldest community assemblage of microscopic and  
22  
23 37 macroscopic biota in the aftermath of the 'Great Oxidation Event', widening our  
24  
25 38 understanding of biological organization during Earth's middle age.  
26  
27  
28  
29  
30

## 31 **Introduction**

32  
33 41 The Paleoproterozoic Era hosted one of the most important geochemical events in Earth's  
34  
35 42 history, marked by a measurable accumulation of atmospheric oxygen, the so-called 'Great  
36  
37 43 Oxidation Event' (GOE) between 2.45–2.32 billion years ago (Ga). Evidence for the GOE  
38  
39 44 comes from the disappearance of detrital pyrite, uraninite and siderite from fluvial and deltaic  
40  
41 45 deposits, an increase in the retention of iron in paleosols, an enrichment of Cr and U in iron  
42  
43 46 formations, and perhaps most importantly, the disappearance of sedimentary sulfur isotope  
44  
45 47 mass-independent (S-MIF) anomalies indicative of atmospheric  $\text{SO}_2$  processing in the  
46  
47 48 absence of appreciable ozone (Holland, 2002; Bekker *et al.*, 2004; Farquhar *et al.*, 2011;  
48  
49 49 Konhauser *et al.*, 2011; Partin *et al.*, 2013a; Lyons *et al.*, 2014). In the wake of the GOE,  
50  
51 50 large positive excursions in the  $\delta^{13}\text{C}$  of marine inorganic carbon, during the 'Lomagundi  
52  
53 51 Event' *ca.* 2.22–2.1 Ga (Karhu & Holland, 1996), is believed to reflect large-scale burial of  
54  
55  
56  
57  
58  
59  
60

1  
2  
3 52 organic matter in marine sediments (Berner, 2004; Bekker & Holland, 2012). New evidence  
4  
5 53 suggests that the ‘Lomagundi Event’ ended with a drastic drop in Earth’s oxygen content (*e.g.*  
6  
7 54 Partin *et al.*, 2013b), perhaps related to large-scale oxidation of organic carbon (Canfield *et*  
8  
9 55 *al.*, 2013) and/or changes in ocean biogeochemical processes that may have inhibited primary  
10  
11 56 productivity (Chi Fru *et al.*, 2015).

13 57 The Francevillian sedimentary rocks *ca.* 2.1 Ga record these biogeochemical  
14  
15 58 fluctuations in Earth’s oxygen accumulation dynamics through extreme excursions in the  
16  
17 59 carbon cycle, in addition to hosting the oldest large colonial macroorganisms (El Albani *et al.*,  
18  
19 60 2010, 2014). Major elements, trace metals, organic carbon and isotope analyses offer  
20  
21 61 constraints on the basin geochemistry, revealing variations from the base to the top that are  
22  
23 62 linked to sea level changes (Canfield *et al.*, 2013; Bankole *et al.*, 2016). The Lower  
24  
25 63 Francevillian fluviatile rocks were deposited in oxygenated waters (Bankole *et al.*, 2016),  
26  
27 64 whereas the Upper Francevillian marine rocks were deposited in oxic, ferruginous and euxinic  
28  
29 65 waters (Canfield *et al.*, 2013). The large macrofossils are highly variable in terms of size,  
30  
31 66 shape and pyritization process being represented by lobate, elongated and rod-shaped as well  
32  
33 67 as disk-shaped morphotypes. The pyritization process did not fully occur in the circular disks,  
34  
35 68 indicating that their organic composition differs from that of pyritized specimens (El Albani *et*  
36  
37 69 *al.*, 2010, 2014). In addition, some carbonaceous spheroidal microstructures have also been  
38  
39 70 reported as organic-walled acritarchs that might have a planktonic origin.

41  
42  
43 71 Recently, microbial fossils were found in the Francevillian sequence, including  
44  
45 72 putative bacteriomorphous structures (Dubois *et al.*, 2015) and a Gunflint-type assemblage of  
46  
47 73 microfossils in the stromatolitic units (Lekele Baghekema *et al.*, 2017). The presence of  
48  
49 74 colonial macroorganisms and microfossils makes the Francevillian biota unique, but  
50  
51 75 interestingly, evidence of microbial mats has never been demonstrated. In this work, we  
52  
53 76 describe for the first time ever microbial mat-related structures (MRS) from 2.1 Ga  
54  
55  
56  
57  
58  
59  
60

1  
2  
3 77 siliciclastic sandstones and black shales from the FB2 Member of the Francevillian basin,  
4  
5 78 Gabon. MRS are physical remains of destroyed mats and structures associated with decay,  
6  
7 79 instead of well-preserved mat growth features (Eriksson *et al.*, 2010). Their sedimentary  
8  
9 80 features are preserved because microbes secrete extracellular polymeric substances (EPS), an  
10  
11 81 adhesive mucilage (Decho, 2000), that provide a coherent and protective coating that is  
12  
13 82 unlikely to arise in sediments without a biological input (Gerdes *et al.*, 1993, 2000; Porada &  
14  
15 83 Bouougri, 2007; Noffke, 2010).

16  
17  
18 84 Microbial life in the Paleoproterozoic has been poorly described (Davies *et al.*, 2016)  
19  
20 85 even though existing paleontological and biogeochemical evidence points towards the  
21  
22 86 existence of significant microbial diversity previously in the Archean. Through a combination  
23  
24 87 of macroscopic and microtexture analyses, petrographic, geochemical, organic elemental  
25  
26 88 analyses and stable carbon isotope composition of bulk organic matter, we compare modern  
27  
28 89 and fossil mat-related structures, in order to characterize the marine paleoenvironment in  
29  
30 90 which the putative microbial mats formed. The data reveal the biogenicity of these structures,  
31  
32 91 adding new insights into the origins of the Francevillian biota (El Albani *et al.*, 2010; Ossa  
33  
34 92 Ossa, 2010; Parize *et al.*, 2013; El Albani *et al.*, 2014; Ngombi Pemba, 2014; Reynaud *et al.*,  
35  
36 93 2017). Importantly, we assessed and described the organisational, ecological and  
37  
38 94 taphonomical processes that led to the development and preservation of the unique  
39  
40 95 Francevillian biota.

## 41 42 43 44 45 46 97 **Geological background**

47  
48 98 The Francevillian basin, located in the southeastern part of the Republic of Gabon (Figure 1a),  
49  
50 99 is a 35,000 km<sup>2</sup> depression comprising 2.2-2.0 Ga marine sedimentary rocks that  
51  
52 100 unconformably overly an Archean basement (Weber, 1969). Petrographic and geochemical  
53  
54 101 analyses indicate that the Francevillian sediments were not affected by metamorphic

1  
2  
3 102 transformation (maximum temperature 100 °C; Gauthier-Lafaye & Weber, 1989; Ngombi-  
4  
5 103 Pemba *et al.*, 2014), resulting in the preservation of seawater composition at the time when  
6  
7 104 deposition took place. Moreover, carbon isotopic and redox sensitive element compositions  
8  
9 105 suggest that the ‘Lomagundi Event’ was a global event (Canfield *et al.* 2013).

10  
11 106 The basin fill, composed of siliciclastic fluvial and marine deposits that are 1000–2500  
12  
13 107 m thick, is subdivided into four major lithostratigraphic formations, FA to FD (Figure 1b;  
14  
15 108 Weber, 1969; Gauthier-Lafaye & Weber, 1989; Gauthier-Lafaye, 2006; El Albani *et al.*, 2010,  
16  
17 109 2014). Fluvial to deltaic conglomeratic sandstones, overlain by marine sandstones  
18  
19 110 deposited in a tidal environment (i.e., syntectonic filling), make up the FA Formation, with  
20  
21 111 the overlying sediments hosting diagenetic uranium ore deposits and the natural nuclear  
22  
23 112 fission reactors of Oklo (Gauthier-Lafaye & Weber, 1989, 2003). The marine-dominated FB  
24  
25 113 sequence rests unconformably on FA. The former was deposited below storm wave base  
26  
27 114 during basin deepening, and is subdivided into the FB1 (a, b and c) and FB2 (a and b)  
28  
29 115 subunits. The FB1a and FB1b subunits are composed of interbedded shales, sandstones and  
30  
31 116 conglomerate, stacked into fining upwards packages, while the overlying FB1c subunit  
32  
33 117 mainly consists of black shales with a thin iron formation, likely corresponding to a maximum  
34  
35 118 flooding surface. This is then overlain by thick Mn-rich carbonates. Massive sandstone beds  
36  
37 119 of the FB2a subunit, probably deposited in channels near the fair-weather wave base, are  
38  
39 120 capped by thinly laminated black shales that are 5 m thick, and interbedded with thin siltstone  
40  
41 121 layers (FB2b), presumably deposited by waning storm surges. Outcrops of the FB2b subunit  
42  
43 122 are scarce but host the well-known colonial macroorganisms described in El Albani *et al.*  
44  
45 123 (2010, 2014). The overlying FC Formation consists of dolomite and thickly-banded  
46  
47 124 stromatolitic cherts that were deposited under shallow-water conditions (Bertrand-Sarfati &  
48  
49 125 Potin, 1994). The uppermost FD Formation consists mainly of black shales, with pyroclastic  
50  
51 126 material at the top deposited in a deep marine environment (Gauthier-Lafaye & Weber, 2003).

1  
2  
3 127 The Francevillian basin has been intensively studied because of economic interests in  
4  
5 128 their uranium and manganese ore content (Gauthier-Lafaye & Weber, 1989, 2003).  
6  
7 129 Consequently, various ages have been obtained for the Francevillian sediments. For example,  
8  
9 130 monazites contained in Archean plutonic rocks from the Chaillu massif close to the FA  
10  
11 131 Formation transition provided U-Pb ages of  $2998 \pm 25$  Ma to  $2621 \pm 30$  Ma (Mouélé *et al.*,  
12  
13 132 2014). A U-Pb age of  $2050 \pm 30$  Ma reported for uranium mineralization, delineates early  
14  
15 133 diagenesis at the FA-FB boundary (Gancarz, 1978). Coarse-grained syenites of the N’Goutou  
16  
17 134 volcanic complex, in the northern part of the Republic of Gabon, that are interlayered with  
18  
19 135 rocks at the base of the FB1 sequence, yield an Rb-Sr age of  $2143 \pm 143$  Ma (Bonhomme *et*  
20  
21 136 *al.*, 1982). It is considered that these volcanic rocks were formed simultaneously with the  
22  
23 137 sedimentary rocks. Diagenetic illites from the top of the FB1b subunit have been dated at  
24  
25 138  $2099 \pm 115$  Ma by using the Sm-Nd method (Bros *et al.*, 1992). Finally, recent dating of  
26  
27 139 zircons from welded tuffs near the top of the FD Formation produced a U-Pb age of  $2083 \pm 6$   
28  
29 140 Ma (Horie *et al.*, 2005).  
30  
31

32  
33 141 The Paleoproterozoic Francevillian MRS were discovered in the Moulendé quarry, the  
34  
35 142 same fossiliferous quarry where large colonial organisms have been reported (El Albani *et al.*,  
36  
37 143 2010, 2014). MRS are heterogeneously distributed in the Upper FB2a subunit, as well as in  
38  
39 144 the overlying laminated black shale. The latter is 5 m thick and forms the FB2b subunit  
40  
41 145 (Figure 2), covering a ~20 m thick host interval.  
42  
43  
44 146

## 45 46 147 **Methods**

### 47 48 148 **Sampling and sample preparation**

49  
50  
51 149 About one hundred samples were collected in order to describe large-scale variability in  
52  
53 150 morphology, structural organization and diversity from outcrops localized in one locality over  
54  
55 151 several years (Figure 1). All samples were logged to provide information on their spatial and  
56  
57  
58  
59  
60

1  
2  
3 152 time repartitions of the studied area (Figure 2), and then photographed at the University of  
4  
5 153 Poitiers using a Nikon Europe D610 digital single-lens reflex camera equipped with a Nikon  
6  
7 154 AF-S 24-120 mm f/4G ED VR lens. Polished slabs were observed using a ZEISS  
8  
9 155 Discovery.V8 stereoscope combined with Axio Cam ERc 5s microscope camera. Based on  
10  
11 156 this pre-screening analysis, representative samples were selected and powdered in an agate  
12  
13 157 mortar for elemental and carbon isotope systematics.  
14  
15  
16 158

### 18 159 Petrographic and mineralogical analysis

20 160 Petrographic and mineralogical examinations were performed by transmitted and reflected  
21  
22 161 light on eight polished thin sections using a Nikon ECLIPSE E600 POL microscope equipped  
23  
24 162 with a Nikon Digital Sight DS-U1 camera and NIS-Element D software for scanning  
25  
26 163 observations. Seven thin sections were carbon coated and examined for textural and  
27  
28 164 compositional analyses using a FEI Quanta 200 scanning electron microscope (SEM) at the  
29  
30 165 University of Lille 1. The SEM, coupled to Rontec energy-dispersive spectra (EDS) for semi-  
31  
32 166 quantitative mineral analysis in backscattered electron mode (BSE), was operated at 15 kV  
33  
34 167 accelerating volts and a 1 nA beam current at a working distance of 10.5 mm.  
35  
36 168

### 40 169 Carbon analysis

42 170 Raman spectroscopy was used to determine the composition of carbon preserved within the  
43  
44 171 MRS on two representative samples. Analyses were carried out at the University of Poitiers  
45  
46 172 with a HORIBA JOBIN YVON Labram HR800UV, an integrated Olympus confocal  
47  
48 173 microscope coupled to a Peltier-cooled CCD detector. All analyses were performed by means  
49  
50 174 of 514.5 nm Ar<sup>+</sup> laser of 1 mW, 200 µm confocal hole, 1800 grooves/mm grating. Data  
51  
52 175 recording and treatment were done with LabSpec 5 software.  
53  
54

55 176 Ten representative samples, composed of five mat samples and five associated  
56  
57  
58  
59  
60



1  
2  
3 177 surrounding sediments, were crushed for the determination of the elemental content of  
4  
5 178 associated organic matter, as well as carbon and sulfur composition, at the University of  
6  
7 179 Poitiers. Analyses were performed using a CHNS analyser, model FlashEA 1112  
8  
9 180 (ThermoFisher Scientific) by flash dynamic combustion at 970 °C under a constant flow of  
10  
11 181 helium. Data were recorded using Eager 300 software. A calibration curve was obtained with  
12  
13 182 sulfanilamide and BBOT – 2,5-Bis(5-tert-butyl-benzoxazol-2-yl)thiophene – before each  
14  
15 183 analysis. The results of carbon contents include both inorganic and organic carbon, but  
16  
17 184 petrographic analyses showed that calcium carbonate and dolomite concentrations were low.

18  
19  
20 185 Stable carbon isotope measurements ( $^{12}\text{C}$ ,  $^{13}\text{C}$ ) of organic matter from 14 mat samples  
21  
22 186 (from both FB2a and FB2b subunits) were conducted at the Stable Isotopes Laboratory of  
23  
24 187 UMR Pegase (INRA Rennes, France), using an elemental analyser coupled with an isotope  
25  
26 188 ratio mass spectrometer (IRMS) (VG Isoprime; UMR PEGASE – INRA Rennes). More than  
27  
28 189 500 mg of fine-grained powders were analysed and loaded in tin capsules for each sample.  
29  
30 190 IAEA-C6 (sucrose ANU,  $\delta^{13}\text{C} = -10.63\%$ ), USGS-24 (graphite,  $\delta^{13}\text{C} = -15.98\%$ ), USGS-40  
31  
32 191 (glutamic acid,  $\delta^{13}\text{C} = -26.32\%$ ) and Urea Isotopic Working Standard ( $\delta^{13}\text{C} = -38.3\%$ ) were  
33  
34 192 used as reference standards. Data are expressed as delta values (‰) relative to Vienna Pee  
35  
36 193 Dee Belemnite (V-PDB). No correction was added to the measured values, and the analytical  
37  
38 194 uncertainty is estimated to be lower than 0.2‰.  
39  
40  
41  
42  
43

#### 44 196 **Facies analysis of the Moulendé Quarry**

45  
46 197 The Moulendé quarry has been examined over an area of ~ 5 ha, for a total of nine studied  
47  
48 198 outcrops (Figure 3a). Among them, the F8 outcrop (Figure 3a-c) was logged in detail because  
49  
50 199 of its well-exposed strata and sedimentary structures. It is the only outcrop where the FB2a-  
51  
52 200 FB2b transition is observed with accompanying black shale deposits. Lithological  
53  
54 201 composition, vertical facies relationships and sedimentary features allow recognition of two  
55  
56  
57  
58  
59  
60

1  
2  
3 202 depositional facies from the MRS-bearing strata.  
4

5 203  
6

7 204 Facies 1  
8

9  
10 205 Thick-bedded, coarse-grained sandstones represent the main facies of the Moulendé quarry.  
11

12 206 These deposits are commonly referred to the Poubara sandstones (FB2a subunit; Figures 2,  
13

14 207 3a-c). This facies is 15 m thick in the quarry, as well as in the closest drill core (GR5; Azziley  
15

16 208 Azzibrouck, 1986), but could be up to 100 m thick elsewhere in the basin (Weber, 1969).  
17

18 209 Interbedded thin-bedded, coarse-grained sandstones and laminated black shales form  
19

20 210 heterolithic beds. The uppermost massive sandstone bed is laterally heterogeneous in  
21

22 211 thickness and its bedding surface is undulatory. At the top of several massive sandstone beds,  
23

24 212 sedimentary features, including load structures, sandstone clasts and water escape structures,  
25

26 213 such as dishes, are present. These beds occasionally contain dm-scale hummocky cross  
27

28 214 stratification (HCS), restricted to the upper part of the succession (Figures 2, 3d; Reynaud *et*  
29

30 215 *al.*, 2017).  
31

32 216  
33

34  
35  
36 217 Facies 2  
37

38 218 Numerous thin-bedded, parallel-laminated black shales with interbeds of siltstones lie  
39

40 219 conformably upon Facies 1. They form stacks of variable thickness in the upper part of the  
41

42 220 studied succession and are about 5 m thick. Connected to the underlying facies and  
43

44 221 approximately 0.4 m in height, a sandstone dyke cross-cuts these multilayered black shales  
45

46 222 (Figures 2, 3e). There is no evidence of fracturing along the dyke, indicating that the  
47

48 223 sediments were not consolidated prior to injection. The main component of facies 2 is  
49

50 224 characterized by rhythmic successions of mm-scale light and dark laminae of siltstones and  
51

52 225 shales. Small-scale cross-laminae are found within mm-thick interbedded siltstones. Load-  
53

54 226 shaped and flame-shaped structures forming convolute bedding (Figures 2, 3f) are observed in  
55  
56  
57  
58  
59  
60

1  
2  
3 227 interbedded medium-to-coarse-grained siltstone beds ranging from 2 to 5 cm in thickness.  
4  
5 228 Interference ripples are also observed, indicating paleowaves coming from two directions  
6  
7 229 (Figures 2, 3g). Lastly, a dm-scale bed containing dark-coloured convex laminae associated  
8  
9 230 with cm-scale current ripples comprise the thickest interbedded coarse-grained siltstones  
10  
11 231 (Figures 2, 3h).

12  
13 232

### 14 15 233 Interpretations

16  
17  
18 234 The variation in thickness of the uppermost massive sandstone level (at ~15 m in the  
19  
20 235 stratigraphy) may be related to detachment folds and troughs later infilled by overlying  
21  
22 236 sediments (Reynaud *et al.*, 2017). Sudden and rapid deposition of coarse-grained sediments  
23  
24 237 produce load and dish structures by immediate dewatering (Reineck & Singh, 1980). Rapid  
25  
26 238 sedimentation also results in sandstone dykes formed by elevated pore pressures leading to  
27  
28 239 fluidization of the unconsolidated sediment. In addition, conditions that are favourable for the  
29  
30 240 formation of HCS are commonly found between the fair-weather and storm wave base  
31  
32 241 (Immenhauser, 2009). Various interpretations have been proposed for the paleoenvironmental  
33  
34 242 setting of the FB2a subunit. They range from a deltaic paleoenvironment subjected to tidal  
35  
36 243 influence (El Albani *et al.*, 2010; Ossa Ossa, 2010), to a shoreface paleoenvironmental setting  
37  
38 244 (Ngombi Pemba, 2014), to a turbidite lobe setting in waters deeper than 200 m (Parize *et al.*,  
39  
40 245 2013). Reynaud *et al.* (2017) showed that the Poubara sandstones are composed of high-  
41  
42 246 density sediment gravity flow deposits, emplaced during a forced regressive system tract.  
43  
44 247 These authors underline that the Francevillian basin was likely isolated because of the absence  
45  
46 248 of wave deposits. They also noticed the presence of linguoid and interference ripples that is  
47  
48 249 consistent with shallow water settings.

49  
50  
51  
52  
53 250 Thinly laminated black shales are deposited in a relatively quiet water setting but  
54  
55 251 interrupted by quickly deposited supplies of millimetre-to-centimetre-scale siltstones. These

1  
2  
3 252 laminae host many sedimentary structures that indicate a strong current. Reynaud *et al.* (2017)  
4  
5 253 suggest that these sediments were deposited close to the maximum regressive surface whereas  
6  
7 254 Parize *et al.* (2013) argue for the deposition of turbidites on an upper slope setting.  
8  
9  
10 255

## 11 256 **Mat-related structures (MRS) in the FB2 Member**

12  
13  
14 257 The MRS documented here come from a 20 m thick interval of the FB2 sequence (Figure 2).  
15  
16 258 Some specimens are entirely or partially pyritized, while others display a few isolated pyrite  
17  
18 259 grains within the mat layers. Following the classification scheme by Sarkar *et al.* (2008), the  
19  
20 260 Francevillian MRS are divided into two major categories: (1) mat-layer structures,  
21  
22 261 representing potential in situ growth of a microbial mat (Figures 4-5, Figure S1) and (2) mat-  
23  
24 262 protected structures (Figure 6), possibly formed by abiotic processes but requiring the  
25  
26 263 protection of a microbial mat (Davies *et al.*, 2016).  
27  
28  
29 264

### 30 31 265 1. Mat-layer structures

32  
33  
34 266 This group of MRS represents the “mat-layer itself that may be intact, deformed or rafted”  
35  
36 267 (Sarkar *et al.*, 2008). In this work, we interpret well-preserved, intact mat growth according to  
37  
38 268 the following criteria.  
39  
40 269

#### 41 42 270 1a. ‘Elephant-skin’ textures

##### 43 44 271 Description

45  
46 272 ‘Elephant-skin’ textures (Runnegar & Fedonkin, 1992) encompass quasi-polygonal,  
47  
48 273 geometrically distinct reticulate patterns, ranging from the millimetre to centimetre scale, and  
49  
50 274 bearing bulges or ridges (Figure 4a-c). They are both identified at the top of the massive  
51  
52 275 Poubara sandstones and the interbedded siltstones in the black shales (Figure 2). Individual  
53  
54 276 polygons are 0.3–1.3 cm in diameter, with a maximum relief of 0.2 cm.  
55  
56  
57  
58  
59  
60

1  
2  
3 277 Microscopic analyses show reticulate patterns preserved as non-homogenous dark  
4  
5 278 laminae above a light, coarser material 200 to 600  $\mu\text{m}$  thick (Figure 7a, f). The overlying  
6  
7 279 layer consists of abundant wavy-crinkly laminae entangling 20 to 50  $\mu\text{m}$  quartz grains and  
8  
9 280 heavy minerals (*e.g.*, titanium oxides, apatites and monazites); the latter suggested by the  
10  
11 281 relative proportions of the elements found through SEM-EDS analysis (Figure S2), as well as  
12  
13 282 transmitted and reflected light microscopy. Most of the grains in the wavy-crinkly laminae are  
14  
15 283 randomly arranged within a clayey matrix, and are dominated by O, Al, Si, Mg, K and Fe  
16  
17 284 (Figure S2; Table S1). Reticulate patterns are also C-rich (up to 8.52%) compared to the  
18  
19 285 underlying sandstone bed, as evident from the Raman (Figure 8a-c) and organic elemental  
20  
21 286 analyses (Table S2). The carbonaceous layer is punctuated by tufted microstructures, either on  
22  
23 287 bulge rims or within the bulges, with similar striking morphologies to each other and where  
24  
25 288 clay layers are almost vertically oriented (Figures 7f, 9a-b). Based upon the description by  
26  
27 289 Noffke *et al.* (2013), the height/base index is 30/100  $\mu\text{m}$  to 120/220  $\mu\text{m}$  long, separated at  
28  
29 290 regular distances of 150 – 230  $\mu\text{m}$  from each other.  
30  
31  
32

33 291

### 35 292 Interpretation

36  
37 293 ‘Elephant-skin’ textures are formed by a specific arrangement of tufts, pinnacles, bulges and  
38  
39 294 smaller-scale bulges arranged into ridges. Tufts, often arising in ridge junctions or at the  
40  
41 295 intersection of microbial bulges, are proposed as a particular type-feature of cyanobacterial  
42  
43 296 mat filaments growing vertically towards a light source (phototaxis) (Gerdes *et al.*, 2000;  
44  
45 297 Porada & Bouougri, 2007; Bose & Chafetz, 2009). These textures are known in modern  
46  
47 298 supratidal environments (Gerdes *et al.*, 2000; Gerdes, 2007; Bose & Chafetz, 2009; Taj *et al.*,  
48  
49 299 2014), but have also been recorded and described in some ancient shallow water  
50  
51 300 environments from the terminal Proterozoic (Runnegar & Fedonkin, 1992; Gehling, 1999),  
52  
53 301 and perhaps even the Archean (Flannery & Walter, 2012). However, Shepard & Sumner  
54  
55  
56  
57  
58  
59  
60

1  
2  
3 302 (2010) debated the role of phototaxis in the formation of reticulate patterns and tufted  
4  
5 303 structures. They investigated whether filamentous cyanobacteria were influenced by light to  
6  
7 304 form polygonal structures or whether they were related to their own morphotype. Thus,  
8  
9 305 reticulate patterns may result from an undirected motility of filamentous bacteria without the  
10  
11 306 influence of light.

12  
13 307

14  
15 308 *1b. Putative macro-tufted microbial mat structures*

16 309 Description

17  
18  
19  
20 310 The putative macro-tufted microbial mats are preserved as positive epireliefs that display  
21  
22 311 patches of vertical bump-like structures protruding 0.05–0.2 cm on the upper surface of  
23  
24 312 interbedded, coarse-grained siltstones (Figures 2, 4d).

25  
26 313 Microscopic features seen in longitudinal thin sections reveal that the coarse-grained  
27  
28 314 siltstone is draped by a 50–500  $\mu\text{m}$  thin, dark, clay-rich layer with floating quartz grains  
29  
30 315 (Figure 7b, g-h). These grains are clearly different in size compared to the coarser grains in  
31  
32 316 the underlying sediment. Some clay particles are micaceous and oriented more or less parallel  
33  
34 317 to the bedding plane. Furthermore, it can be noted that the thickness of this overlying dark  
35  
36 318 layer varies along the longitudinal section. The thinner dark-coloured layer is found at the top  
37  
38 319 of the microtopography, whereas the thicker one overlies the troughs.

39  
40  
41 320 SEM imaging reveals that the dark lamina encompasses heterogeneously-sized, 5–40  
42  
43 321  $\mu\text{m}$  quartz grains and heavy minerals (Figure 9c), while clay minerals are positioned sub-  
44  
45 322 vertically. In addition, EDS analyses suggest that these laminated minerals are mainly made  
46  
47 323 of O, Si, Al, K elements, with minor Mg, Fe and Na (Table S1), consistent with the elemental  
48  
49 324 composition of mica and illite minerals (*e.g.* Velde & Meunier, 2008).

50  
51 325

52  
53 326 Interpretation

1  
2  
3 327 A similar macro-tufted microbial mat was recorded from a 2.0 Ga paleodesert environment  
4  
5 328 where 0.2 cm high mound-like structures are randomly arranged on a fine-grained sandstone  
6  
7 329 (Simpson *et al.*, 2013). The mechanism behind the development of this feature in the  
8  
9 330 sedimentary rock record remains unclear. However, by changing the polarity of their  
10  
11 331 filamentous structure, the growth of a microbial biofilm is able to produce similar bump-like  
12  
13 332 structures in modern sedimentary environment (Gerdes *et al.*, 2000; Gerdes, 2007; Bose &  
14  
15 333 Chafetz, 2009; Taj *et al.*, 2014). This pattern may also result from the direct filling of the pre-  
16  
17 334 existing microtopography by mat-building organisms as they grow and expand (Simpson *et*  
18  
19 335 *al.*, 2013). The smooth but bumpy morphology is likely enhanced by syndepositional loading  
20  
21 336 and post-depositional compaction, and so this bio-sedimentary expression could be viewed as  
22  
23 337 a combined microbial and compaction feature.  
24  
25  
26  
27  
28

29 339 1c. *Domal buildups*

30  
31 340 Description

32  
33 341 Domal buildups are preserved as positive bed-top features on bedding surfaces of black shales  
34  
35 342 (Figure 2). They are characterized by 0.1–0.4 cm convex, domal structures projecting  
36  
37 343 upwards from the bedding plane. Distinctive features include a cluster of low mound-shaped  
38  
39 344 structures, 0.4 cm in diameter, nearly equal in all instances and without any central  
40  
41 345 depressions (Figure 4e-f). Alternatively, they can be isolated structures with a diameter  
42  
43 346 ranging from 0.7 cm to 1.5 cm that seem to reveal a cauliflower-like texture associated with  
44  
45 347 extensive positive-relief, wrinkled structures (Figure 4g). Circular disks belonging to the  
46  
47 348 oldest large colonial organisms (El Albani *et al.*, 2014) seem closely associated with these  
48  
49 349 specific structures. Both isolated and clustered domal structures have been shown to be  
50  
51 350 pyritized (Table S2). Bulk sulfur level of up 22.16% within the domal structures is associated  
52  
53 351 with a carbon content <0.53%. There are also flat, pyritized mat-related structures without any  
54  
55  
56  
57  
58  
59  
60

1  
2  
3 352 particular distinctive features that tend to develop close to the clustered domes (Figure 4f,  
4  
5 353 Figure S1).

6  
7 354 Thin sections reveal a well-defined alternation of clay and silt layers beneath the  
8  
9 355 domal structures (Figure 7c). Most of the quartz particles from the underlying sediment are  
10  
11 356 laminated and/or have a length of grain-to-grain contact of mostly 20–80  $\mu\text{m}$ . None of these  
12  
13 357 grains were found in the topmost dark, clay layer. Furthermore, the domal structures typically  
14  
15 358 show an indication of internal convex lamination between all pyrite grains (Figure 7i), which  
16  
17 359 reflects the position of the domes in epirelief.

18  
19  
20 360  
21  
22 361 Interpretation

23  
24 362 Domal buildups have been reported from fluvial and fluviodeltaic settings in Mid-Proterozoic  
25  
26 363 (Garlick, 1988; Schieber, 1998, 1999; Sheldon, 2012; Wilmeth *et al.*, 2014) to shallow water  
27  
28 364 settings in Late Cambrian times (Bottjer & Hagadorn, 2007). The latter authors proposed that  
29  
30 365 they “may represent different life histories, biological affinities, and/or histories of interaction  
31  
32 366 with the physical environment”. Previous studies have also invoked a distinct mat growth  
33  
34 367 pattern (Wilmeth *et al.*, 2014) and inferred that domal structures are built by an upward  
35  
36 368 growth of microbial mats. This might reflect competition for light (Garlick, 1988; Schieber,  
37  
38 369 1999). The  $\delta^{13}\text{C}_{\text{org}}$  isotopic signatures of Mesoproterozoic domal-like structures in Copper  
39  
40 370 Harbor Conglomerate (Upper Peninsula of Michigan) are attributed to photosynthesis  
41  
42 371 (Sheldon, 2012).

43  
44  
45 372 EPS possess chemical properties that protect cells by creating sharp geochemical  
46  
47 373 gradients (Decho, 2000), while the anaerobic decay of the buried mat material facilitates the  
48  
49 374 precipitation of diagenetic minerals such as pyrite, depending on sulfate and iron  
50  
51 375 bioavailability. If this diagenetic mineralization follows individual layers within the EPS  
52  
53 376 demarcated boundaries, or if it is associated with specific features, the former presence of  
54  
55  
56  
57  
58  
59  
60



1  
2  
3 377 microbial mats are overprinted and preserved as a mineralized signature (Schieber, 1999).  
4  
5 378 Thus, sulfate-reducing microorganisms probably used the carbonaceous material from the  
6  
7 379 domal buildups as their electron donor, thereby releasing hydrogen sulfide to react with  
8  
9 380 available iron. This mechanism is supported by the recurrent low carbon to high sulfur  
10  
11 381 contents in the materials. Analyses of the sulfur isotope contained in pyrite from the  
12  
13 382 Francevillian series measured by Secondary Ion Mass Spectrometry (SIMS) further revealed  
14  
15 383 negative  $\delta^{34}\text{S}$  values associated with widespread microbial decay, linked to the activities of  
16  
17 384 the sulfate-reducing microorganisms (El Albani *et al.*, 2014).  
18  
19  
20  
21

#### 22 386 1d. *Discoidal microbial colonies*

##### 23 24 387 Description

25  
26 388 A discoidal microbial colony (Grazhdankin & Gerdes, 2007) is a term for a mat-layer that  
27  
28 389 includes disk-shaped, internal, centimetre-scale features (Figure 5a-g). Two major distinct  
29  
30 390 discoidal microbial colony-like morphologies occur on bedding planes in the black shale unit  
31  
32 391 (Figure 2). The first is characterized by centimetre to the decimetre scale clusters of outward-  
33  
34 392 convex, rod-shaped structures with internal pyritized concentric bands, possessing a series of  
35  
36 393 ~0.4 cm wide light and dark zones (Figure 5a-b). This specific feature does not exhibit any  
37  
38 394 relief. The second variety is made up of well-marked circular bodies represented by sharp  
39  
40 395 outlines separating the specimens from the surrounding black shale (Figure 5c-g). The disk-  
41  
42 396 shaped colonies display slight internal concentric zonations, wrinkle features or a lack of any  
43  
44 397 specific morphological characteristics. A variety of the specimens have a 1.1–1.7 cm high  
45  
46 398 disk-shaped relief with concentric rims restricted to the edges, which may present themselves  
47  
48 399 as cauliflower-like patterns varying between 3.3 and 8.2 cm in diameter (Figure 5c-e). There  
49  
50 400 are numerous distinct large euhedral pyrite crystals on these structures. Less common are  
51  
52 401 disk-shaped bodies of 2.3 cm in diameter and represented by a minor relief, internal  
53  
54  
55  
56  
57  
58  
59  
60

1  
2  
3 402 millimetre-scale wrinkles, and devoid of sharp outlines (Figure 5f). Other observable  
4  
5 403 discoidal structures are relatively small (~ 0.5 cm diameter) that do not have particular  
6  
7 404 features (Figure 5g). However, these are the only structures that are entirely pyritized by tiny  
8  
9 405 pyrite crystals.  
10

11 406

#### 13 407 Interpretation

15 408 Previous studies have shown that a wide range of variability exists in the morphology and  
16  
17 409 organization of modern discoidal microbial colonies in natural environments (Gerdes *et al.*,  
18  
19 410 1993; Banerjee *et al.*, 2014; Sarkar *et al.*, 2014) as well as under laboratory conditions  
20  
21 411 (Matsushita *et al.*, 2004). Concentric zonations with a series of light and dark bands represent  
22  
23 412 a particular variety of discoidal microbial colony known as ‘fairy rings’. Modern ‘fairy ring’  
24  
25 413 structures are ubiquitous in salt marshes (Gerdes *et al.*, 1993; Gerdes, 2007) and in shallow  
26  
27 414 water environments (Banerjee *et al.*, 2014). The concentric ring-shaped structures of the  
28  
29 415 Francevillian series discoidal structures clearly display the same striking morphologies. All  
30  
31 416 modern examples indicate that filamentous cyanobacteria and diatoms, which are embedded  
32  
33 417 in EPS and crowned by micro-pinnacles, form these concentric ring-shaped structures. This  
34  
35 418 arrangement is likely not random but represents an oriented behaviour that might be triggered  
36  
37 419 by external environmental factors (Gerdes, 2007). So far, the generally accepted mechanism  
38  
39 420 of formation involves escaping gas bubbles from the substrate, which may cause concentric  
40  
41 421 wave propagation (Gerdes *et al.*, 1994). Subsequently, chemotactic responses initiated by  
42  
43 422 adapted filamentous cyanobacteria may form the concentric organizational patterns. Presently,  
44  
45 423 the oldest discoidal microbial colonies that have been described are from Mesoproterozoic  
46  
47 424 and Neoproterozoic shallow submarine environments (Grazhdankin & Gerdes, 2007;  
48  
49 425 Banerjee *et al.*, 2010, 2014; Sarkar *et al.*, 2014), where pyritized filamentous structures are  
50  
51 426 sometimes preserved (Grazhdankin & Gerdes, 2007).  
52  
53  
54  
55  
56  
57  
58  
59  
60

1  
2  
3 4274  
5 428 1e. *Horizontal mat growth pattern*6  
7 429 Description8  
9 430 A unique, outward-convex, spindle-shaped structure extending over 34 cm is developed on  
10  
11 431 the bedding plane surface of the black shale unit (Figures 2, 5h). The structure appears similar  
12  
13 432 to the spindle-shaped ‘fairy ring’ structures described above. However, this structure is  
14  
15 433 represented by tiny, 0.1 cm tall, arched ridges, rising horizontally, following a well-defined  
16  
17 434 geometric pattern. These sharp-crested ridges of 0.15 cm in width are regularly spaced,  
18  
19 435 commonly dissected and slightly undulated. It appears that the laminae convexity of the  
20  
21 436 whole structure is unevenly distributed, ranging from 55 to 86 degrees.  
22  
23

24 437

25  
26 438 Interpretation27  
28 439 The horizontal mat growth pattern could be related to ‘fairy ring’ structures with which the  
29  
30 440 pattern shares some similarities (*e.g.* outward-convex, spindle-shaped, sharp-crested ridges).  
31  
32 441 Nevertheless, there are no alternations of light and dark zones. Processes implicated in the  
33  
34 442 formation of ‘fairy ring’ structures may be involved here, but topography is added. The  
35  
36 443 orientation of the wave propagation and subsequent millimetre-sized ripples may be induced  
37  
38 444 by gravity. Then, pinnacle-forming organisms would interact with the nutrient front by  
39  
40 445 chemotactic responses to colonize the substratum, producing the distinct morphology  
41  
42 446 preserved in the sedimentary record. Alternatively, localized mat failure and strain induced by  
43  
44 447 gravity, waves or currents could also explain the morphology as a mechanical deformation of  
45  
46 448 biogenically stabilized sediment. Although it has not been suggested in other studies,  
47  
48 449 morphological features including a point of origin, persistent “growth” in one vector, and  
49  
50 450 sharp boundaries could also be explained by an underwater seep that is confined by a biomat  
51  
52 451 and promotes mat growth in a downslope direction. In any case, the parallel arrangement of  
53  
54  
55  
56  
57  
58  
59  
60

1  
2  
3 452 ridges, as well as the regularity of components in the horizontal mat growth pattern, suggests  
4  
5 453 a biotic origin.

6  
7 454

## 8 9 455 2. Mat-protected structures

10  
11 456 This category of mat-related structures arises from structures that probably require mats for  
12  
13 457 their preservation, the exception being wrinkle marks.

14  
15  
16 458

### 17 18 459 2a. *Wrinkle structures*

#### 19 20 460 Description

21  
22 461 Based on morphology, three types of wrinkle structures are categorized here: wrinkle marks,  
23  
24 462 parallel wavy wrinkle structures and cross-cutting wrinkle structures. Wrinkle marks are  
25  
26 463 represented as laterally continuous or discontinuous, slight, outward-convex positive relief on  
27  
28 464 bedding plane of the black shales (Figures 2, 4h).

29  
30  
31 465 Parallel wavy wrinkle structures are preserved as sinuous, continuous ridges separated  
32  
33 466 by parallel, narrow valleys extending for less than 10 cm on bedding surfaces of sandstones  
34  
35 467 and interbedded thin-to-medium-bedded siltstones (Figures 2, 6a-b). The ridges have rounded  
36  
37 468 tops and steep sides, with an individual ridge elevation of 0.1 cm and a spacing of 0.4 cm.  
38  
39 469 Organic elemental analysis of one sample from the black shale unit does not reveal significant  
40  
41 470 differences in carbon content between the parallel wavy wrinkle structures and the  
42  
43 471 surrounding sediment (Table S2). However, microscopic analysis of thin sections, cut  
44  
45 472 perpendicularly through the wrinkles, indicates that a dark-coloured layer caps the coarse, silt-  
46  
47 473 sized rippled structures. Further down, the sediment displays quasi-planar laminations (Figure  
48  
49 474 7d). For the length of the section, the topmost carbonaceous layer is similar in thickness and  
50  
51 475 does not onlap the rippled bed, but instead reproduces its topography (Figure 7j). Oriented  
52  
53 476 quartz grains trapped within the carbonaceous layer (Figure 7j) appear to have the same grain  
54  
55  
56  
57  
58  
59  
60

1  
2  
3 477 size as those found in the rippled structure. Tiny floating grains are also embedded in the clay-  
4  
5 478 sized fractions. Sheets of various clay particles entangle several heavy minerals, mainly  
6  
7 479 titanium oxides (Table S1).

8  
9 480 Cross-cutting wrinkle structures (Banerjee & Jeevankumar, 2005) are characterized by  
10  
11 481 bifurcating and frequently interconnected asymmetric ridges with intervening sub-parallel  
12  
13 482 troughs on the bedding surface of black shales (Figures 2, 6c). The rounded ridges are 0.1 to  
14  
15 483 0.2 cm high, 0.4 to 0.5 cm wide, and their spacings vary from 0.4 to 1 cm. A few dome-like  
16  
17 484 structures of 0.5 to 0.6 cm are close to these cross-cutting wrinkle structures (Figure 6c).

#### 18 485 19 20 21 22 486 Interpretation

23  
24 487 Wrinkle structures are one of the most common sedimentary features related to microbial  
25  
26 488 mats. They are found over a large paleogeographic range, including the deep-sea (Buatois &  
27  
28 489 Mángano, 2003; Flood *et al.*, 2014), shallow marine (Hagadorn & Bottjer, 1997; Banerjee &  
29  
30 490 Jeevankumar, 2005; Sarkar *et al.*, 2006; Porada & Bouougri, 2007; Mata & Bottjer, 2009;  
31  
32 491 Banerjee *et al.*, 2014; Buatois *et al.*, 2014; Sarkar *et al.*, 2014, 2016; Yang *et al.*, 2017),  
33  
34 492 fluvial and lacustrine (Chu *et al.*, 2015, 2017), and even continental environments (Simpson *et*  
35  
36 493 *al.*, 2013). Some researchers claimed that relative microbial community growth correlates to  
37  
38 494 with irregular surface of wrinkle structures (Hagadorn & Bottjer, 1997; Banerjee &  
39  
40 495 Jeevankumar, 2005; Sarkar *et al.*, 2006, 2014).

41  
42 496 Loading and dewatering processes have also been proposed for wrinkle generation  
43  
44 497 (Noffke *et al.*, 2002). A recent study has proposed that abiotic mechanisms are unable to  
45  
46 498 create millimetre-scale ripples (3–15 mm wavelengths) because waves with small orbital  
47  
48 499 amplitudes are not strong enough to mobilize sand and silt grains (Mariotti *et al.*, 2014). In  
49  
50 500 wave tank experiments, millimetre-scale ripples were perfectly reproduced by means of  
51  
52 501 microbial aggregates rolling along the substrate and transporting grains. The preservation of  
53  
54  
55  
56  
57  
58  
59  
60

1  
2  
3 502 such structures requires burial by fine material that may be represented by the biostabilization  
4  
5 503 of a bacterial community. The dark-coloured layer overlapping the silt-sized rippled structures  
6  
7 504 (Figure 7d, j) is probably induced by EPS that acts as a trap for particles from the surrounding  
8  
9 505 environment (Hagadorn & Bottjer, 1997). Oriented grains are result of a growing biofilm that  
10  
11 506 envelops, lifts, rotates and orientates the grains (Noffke *et al.*, 1997, 2001). By combining  
12  
13 507 morphological description and petrographic study, it appears that wrinkle structures are  
14  
15 508 polygenic. Both mat-layer and mat-protected structures are therefore most likely represented  
16  
17 509 in this case.  
18  
19

20 510

## 21 511 2b. '*Kinneyia*' structures

### 22 512 Description

23  
24  
25 513 '*Kinneyia*' structures are characterized by clearly distinct, short, sinuous ridges and troughs of  
26  
27 514 0.2 cm in width and less than 0.1 cm in height on the bedding surface of the black shale unit  
28  
29 515 (Figures 2, 6d). These structures fit with the definition of '*Kinneyia*' as proposed by (Porada  
30  
31 516 *et al.*, 2008), *i.e.*, they are "comparatively short, curved, frequently bifurcating, flat-topped  
32  
33 517 crests, 0.5–1 mm high and 1–2 mm wide, which are separated by parallel, round-bottomed  
34  
35 518 depressions. The crests are usually steep sided and may run parallel".  
36  
37  
38  
39

40 519

### 41 520 Interpretation

42  
43  
44 521 The origins of "*Kinneyia*" structures have long been amongst the most problematic to  
45  
46 522 understand. From their initial description as fossil algae (Walcott, 1914) to the present day  
47  
48 523 where the term is now used to describe MRS, they have been interpreted in various ways  
49  
50 524 (Hagadorn & Bottjer, 1997; Noffke *et al.*, 2002; Porada & Bouougri, 2007; Porada *et al.*,  
51  
52 525 2008; Thomas *et al.*, 2013; Mariotti *et al.*, 2014). However, few hypotheses properly explain  
53  
54 526 how the underlying sediment is affected (Davies *et al.*, 2016). Recently, '*Kinneyia*' structures  
55  
56  
57  
58  
59  
60

1  
2  
3 527 were successfully reproduced in wave tank experiments using microbial aggregates (Mariotti  
4  
5 528 *et al.*, 2014), although the sharply defined morphology of the depressions preserved might  
6  
7 529 suggest that gas bubbles formed beneath the biomat could also be a possible mechanism  
8  
9 530 (Pfluger, 1999). It has also been demonstrated that ‘Kinneyia’ is a polygenetic texture (Davies  
10  
11 531 *et al.*, 2016), but the Francevillian ‘Kinneyia’ structures do not rule out formation by biotic  
12  
13 532 mediators.  
14

15  
16 533

### 17 534 *2c. Linear patterns*

#### 18 535 Description

19  
20  
21  
22 536 Linear patterns are characterized by 0.1–0.3 cm high, parallel, linear ridges, slightly undulated  
23  
24 537 on the bedding surfaces of massive sandstones and interbedded siltstones (Figures 2, 6e, g).  
25  
26 538 They are of varying size, ranging from 2 to 8 cm in length and 0.3 to 0.7 cm in width. Around  
27  
28 539 these linear ridges, the surface morphology is not uniformly flat but bears micrometric spots  
29  
30 540 that seem to be embedded in the matrix (Figure 6f). Furthermore, Raman spectrometry  
31  
32 541 indicates this dark-coloured layer is carbon-rich compared to the underlying sediments  
33  
34 542 (Figure 8d-e).  
35  
36

37 543 Microscopic observations reveal that the 100 to 300  $\mu\text{m}$  thick, carbon-rich layer lies on  
38  
39 544 lighter, sand-sized quartz grains and consists of multiple, well-defined sheets of clay minerals  
40  
41 545 (Figure 7e, k). SEM imaging shows that numerous small quartz grains and heavy minerals,  
42  
43 546 such as apatite, titanium oxide and zircon, are embedded in the clay matrix (Figure 9d-e). This  
44  
45 547 matrix is formed by O, Si, Al, Mg, Fe and K elements, *i.e.* chlorite and illite, as expressed by  
46  
47 548 EDS analyses (Table S1). Furthermore, sand-sized quartz grains are observed inside the  
48  
49 549 ridges as well as the surrounding sediment but are separated by a clayish undulated layer  
50  
51 550 (Figure 9e). The quartz grains inside the ridges and those from the host rock appear randomly  
52  
53 551 oriented.  
54  
55  
56  
57  
58  
59  
60

552

553 Interpretation

554 According to the identification of linear patterns in modern tidal flats by (Porada & Bouougri,  
555 2007) “straight to irregular ridges are developed at distance of 1–2 cm and are locally  
556 interrupted or reduced to faint lines on the flat mat surface”. Towards the water line, oriented  
557 bacterial filaments dominate these structures. In experimental studies, Shepard & Sumner  
558 (2010) observed linear ridges of up to 15 cm long made of cyanobacterial filaments running  
559 parallel to the incident light. Moreover, it has been proposed that a faint rippled surface may  
560 imply a linear pattern because of the preferential microbial growth following slight ridges  
561 (Bouougri & Porada, 2007; Gerdes, 2007; Porada & Bouougri, 2007).

562 The presence of carbonaceous material within the dark-coloured layer is congruent  
563 with a biotic origin. Microtextures, such as tiny quartz particles and heavy minerals embedded  
564 in the matrix, are caused by the trapping and binding processes related to microbial activity  
565 (Gerdes, 2007; Noffke, 2010). Individual grains bound in the organic matrix can be compared  
566 to those observed with laboratory-grown cyanobacteria. These are described as oriented  
567 grains that are pushed upwards during their growths (Noffke *et al.*, 2001; Noffke, 2010).

568 On a macroscopic level, the Francevillian MRS strongly resemble the linear structures  
569 described above, commonly equivalent in shape but slightly smaller in size. However, no  
570 microscopic features were described until now. Taking microtextures into account, it seems  
571 unlikely that bacterial orientation is capable of mobilizing large amount of sediments to form  
572 ridges. Microbial shrinkage caused by a period of subaerial exposition, is also a possibility  
573 (e.g. Chu *et al.*, 2017; Kovalchuk *et al.*, 2017), although the surface morphologies and  
574 microtextures are not consistent with this process. Also, dilational strain on a mildly dipping  
575 sediment surface could explain these features, but their orientations are irregular and their  
576 distributions are sporadic. Liquefaction underneath the microbial mat, due to a rise in pressure



1  
2  
3 577 (*e.g.* Porada *et al.*, 2007), could have been the cause of these particular ridges but neither  
4  
5 578 sediment rising nor upward-facing microbial laminae beneath the ridges have been observed.  
6  
7 579 Finally, linear patterns may result from two growth periods interrupted by small and rippled  
8  
9 580 sedimentary structures (Figure 9e). This condition might be the best explanation for microbial  
10  
11 581 laminae throughout the linear ridges, and the second mat growth period may have followed  
12  
13 582 the ridge orientation as previously thought (Bouougri & Porada, 2007; Gerdes, 2007; Porada  
14  
15 583 & Bouougri, 2007). Indirectly, linear patterns are considered to be mat-protected structures.  
16  
17  
18 584

#### 20 585 2d. *Nodule-like structures*

##### 22 586 Description

24 587 Nodule-like structures are characterized by an elongated shape approximately 10 cm long and  
25  
26 588 an irregular surface topography on the bedding surfaces of black shales (Figures 2, 6h). The  
27  
28 589 surfaces of nodule-like structures comprise several millimetre-scale, tiny, crinkled ridges that  
29  
30 590 are randomly distributed. Composed of silt-sized grains and capped by a dark-coloured  
31  
32 591 wrinkle layer, the nodule-like structure was observed in a polished slab.  
33  
34

35 592

##### 37 593 Interpretation

39 594 Similar nodular to biscuit-like surface structures have been observed in laboratory-cultured  
40  
41 595 bacteria and in modern supratidal settings (Gerdes, 2007). This atypical morphology is  
42  
43 596 thought to be produced by a relative abundance of coccoid cyanobacteria. However, the  
44  
45 597 Francevillian nodular structures possibly reflect mat-protected structures instead of mat  
46  
47 598 growth structures since the internal part of the nodules is not composed of organic matter but  
48  
49 599 rather of quartz particles.  
50

52 600

### 55 601 3. Isotopic analyses

1  
2  
3 602 The  $\delta^{13}\text{C}$  values (V-PDB) of the organic fraction, measured on different mat morphologies in  
4  
5 603 both sandstone and black shale facies range from -30.67‰ to -41.26‰ (Table 1). These  
6  
7 604 values are similar to previous determinations on the bulk  $\delta^{13}\text{C}$  of the organic matter within the  
8  
9 605 FB2 sequence, varying between *ca.* -35‰ to -30‰ (Gauthier-Lafaye & Weber, 2003;  
10  
11 606 Canfield *et al.*, 2013).

12  
13 607

## 14 15 16 608 **Discussion**

### 17 18 609 **Biogenicity**

19  
20  
21 610 The biogenicity criteria reviewed in Noffke (2009) and Wacey (2009) establishes the  
22  
23 611 investigated mat-like structures to be of a microbial mat origin, having formed on the shallow  
24  
25 612 marginal self-environment of the 2.1 Ga Francevillian basin (Reynaud *et al.*, 2017). The  
26  
27 613 sedimentary facies on which the structures are identified must not have undergone  
28  
29 614 metamorphism beyond greenschist grade (Noffke, 2009). This is in agreement with the  
30  
31 615 absence of metamorphic overprint in the Francevillian facies (maximum temperature 100 °C;  
32  
33 616 Gauthier-Lafaye & Weber, 1989; Ngombi-Pemba *et al.*, 2014). In terms of shape and size, the  
34  
35 617 Francevillian MRS are a perfect match to those described in the Precambrian and the  
36  
37 618 Phanerozoic (Figures S3-S4) in accordance with the size distribution between modern and  
38  
39 619 ancient MRS, which should be comparable (Noffke, 2009). Typically, the taphonomic  
40  
41 620 preservation window of MRS in the sedimentary record is valid, but not restricted by  
42  
43 621 ecological setting (Davies *et al.*, 2016). Noffke (2009) suggested that most MRS are related to  
44  
45 622 photoautotrophic mats formed in well-lit shallow marine environments, preferentially on fine  
46  
47 623 sand deposits, even though recent studies argued that such features can also arise on deep  
48  
49 624 marine sediments that do not receive light (Davies *et al.*, 2016). Regardless, our samples  
50  
51 625 originated from a shallow marine setting associated with rapid sand flow deposits within a  
52  
53 626 well-lit portion of the 2.1 Ga Francevillian continental shelf (Reynaud *et al.*, 2017).

1  
2  
3 627 Microtextural composition of the analysed fabric further support the biological  
4  
5 628 trapping, binding (or 'flypaper' effect) and orientation of grains induced by the growth and  
6  
7 629 development of microbial mats and their hydrologically-controlled interaction with sediments.  
8  
9 630 The Francevillian MRS express this biological process by containing clay particles, floating  
10  
11 631 grains of silt-sized quartz and concentrated heavy minerals, as well as by wavy-crinkly  
12  
13 632 laminae (Figures 7f-k, 9, Figure S2; Table S1). These form well-defined organo-sedimentary  
14  
15 633 structures caused by microbial baffling and trapping. The randomly oriented clay minerals in  
16  
17 634 mat laminae suggest that they were trapped on the mat surface whereas laminated clay  
18  
19 635 particles suggest a probable alignment by compaction (Schieber, 1998). Oriented grains  
20  
21 636 reflect a particular microtexture (Figures 6f, 7j), while grain size matches that of the  
22  
23 637 underlying substratum. It is commonly thought that these particles were dragged upwards by  
24  
25 638 cyanobacterial mat growth (Noffke *et al.*, 1997, 2001).

26  
27  
28 639 In addition, geochemical evidence suggests bacterially induced biological processes  
29  
30 640 characterized by carbonaceous material enriched in light carbon (Figure 8; Table 1) and  
31  
32 641 pyritized structures (Figures 4e-g, 5a-e, g, 7c, i) that are depleted in heavy sulfur. The latter  
33  
34 642 points to diagenetic mat destruction through burial decay (Noffke, 2009; Noffke *et al.*, 2013)  
35  
36 643 and anaerobic respiration of that organic carbon by sulfate-reducing microorganisms (El  
37  
38 644 Albani *et al.*, 2014; Hill *et al.*, 2016).

39  
40  
41 645

#### 42 43 646 **Paleoenvironmental interpretations and implications**

44  
45 647 Modern mat-related structures are mostly described in carbonate and siliciclastic  
46  
47 648 environments but few have been described from shale deposits. The presence of black shales  
48  
49 649 with large amounts of organic matter deposited in the photic zone may arise in restricted to  
50  
51 650 isolated basins (Schwark & Frimmel, 2004). Some anoxygenic photosynthetic bacteria even  
52  
53 651 prospered in these paleoecological conditions and their high productivity may be related to the  
54  
55  
56  
57  
58  
59  
60

1  
2  
3 652 availability of essential nutrients. For any MRS-bearing rocks, the hydraulic pattern must be  
4  
5 653 moderated with a low sedimentation rate to promote the development of microbial  
6  
7 654 communities on a substrate (Schieber, 1999; Gerdes *et al.*, 2000; Gerdes, 2007; Noffke, 2009,  
8  
9 655 2010). As an indicator of paleo-hydrological conditions, clay minerals and silt-sized grains  
10  
11 656 within mat layers, are taken to represent currents strong enough to move thin particles but  
12  
13 657 insufficient to transport sand-sized grains (Schieber, 1998; Noffke, 2009). Silt-sized  
14  
15 658 sedimentary particles and heavy minerals can also be baffled and trapped by cyanobacterial  
16  
17 659 filaments moving vertically upwards in order to escape being buried by the small-sized  
18  
19 660 particles, as well as their need to reach optimal light conditions for growth (Noffke, 2009,  
20  
21 661 2010).

22  
23  
24 662 In this study, some of the mat-like structures, including the ‘elephant-skin’  
25  
26 663 morphotypes, the tufted structures, and the linear patterns, tend to be associated with silty  
27  
28 664 lenses (Figure 2), suggesting that the baffling and grain trapping processes were operating in  
29  
30 665 potential microbial mat-dominated environments at 2.1 Ga. Further, the comparable  
31  
32 666 association of several MRS to the distribution of modern and fossil analogues have been used  
33  
34 667 to improve the reliability of paleoenvironmental marine interpretations, including physical  
35  
36 668 processes such as desiccation and erosion and biological activity (Bose & Chafetz, 2009;  
37  
38 669 Noffke *et al.*, 2013; Banerjee *et al.*, 2014; Sarkar *et al.*, 2014). Importantly, the absence of  
39  
40 670 desiccation and erosion-induced MRS in the Francevillian rocks suggest a quiet underwater  
41  
42 671 environment from the time of deposition to when the sediments were lithified and buried.  
43  
44

45  
46 672 The Paleoproterozoic Francevillian MRS possess a wide spectrum of morphologies  
47  
48 673 that can be related to photoautotrophic microbial assemblages. Indeed, discoidal microbial  
49  
50 674 colonies in the modern environments and domal buildups in ancient settings are results of  
51  
52 675 cyanobacterial chemotaxis or phototaxis behaviours (Gerdes, 2007). The biological  
53  
54 676 mechanisms leading to oriented grains has been reproduced with cultures of cyanobacteria  
55  
56  
57  
58  
59  
60

1  
2  
3 677 (Noffke *et al.*, 2001). Reticulate patterns and tufted microbial mats have striking  
4  
5 678 morphologies with modern analogues built by filamentous cyanobacteria (Figure S3a; Gerdes  
6  
7 679 *et al.*, 2000; Gerdes, 2007; Bose & Chafetz, 2009; Taj *et al.*, 2014). It is thought that their  
8  
9 680 formation implies a phototactic behaviour (Gerdes *et al.*, 2000; Reyes *et al.*, 2013), whereas  
10  
11 681 laboratory-cultured filamentous cyanobacteria show a dependency on oxygen concentration  
12  
13 682 (Sim *et al.*, 2012). It has also been proposed that the undirected gliding motility of  
14  
15 683 filamentous bacteria species may form these structures (Shepard & Sumner, 2010).  
16  
17 684 Consequently, all bacteria with highly motile filaments are believed to be able to display these  
18  
19 685 morphologies. Filamentous sulfur-oxidizing bacteria may also have the ability to produce  
20  
21 686 ‘elephant-skin’-like and tuft-like structures (Flood *et al.*, 2014). However, research by  
22  
23 687 genomic comparisons reveals that these phenotypic traits were most likely inherited by  
24  
25 688 horizontal gene transfers from the cyanobacteria (Flood *et al.*, 2014). In other words, those  
26  
27 689 aerobic chemolithoautotrophs may not have been in existence at 2.1 Ga. In addition, recent  
28  
29 690 studies in a perennially ice-covered Antarctic lake have shown the specific assemblage of a  
30  
31 691 photosynthetic microbial ecosystem (Sumner *et al.*, 2015; Jungblut *et al.*, 2016), with  
32  
33 692 cyanobacteria forming tuft-related structures exclusively found in the oxic zone where  
34  
35 693 irradiance is at its highest, whereas flat bacterial mats of anoxygenic photoautotrophs are  
36  
37 694 restricted to the deeper euxinic zone experiencing lower irradiance. Thus, ‘elephant-skin’ and  
38  
39 695 tufted structures may possibly have a link with oxygenic photoautotrophic microorganisms.  
40  
41 696 Importantly, Flannery & Walter (2012) and Homann *et al.* (2015) thought that cyanobacteria  
42  
43 697 are the only microorganisms capable of producing vertical structures or tufts.  
44  
45  
46  
47  
48  
49

## 50 699 Geomicrobiological implications

51  
52  
53 700 It is well established that carbon fixation by autotrophic organisms preferentially incorporates  
54  
55 701 light  $^{12}\text{C}$  over heavy  $^{13}\text{C}$  isotopes in biomass (Schidlowski, 1988, 2001). In this regard, the  
56  
57  
58  
59  
60

1  
2  
3 702  $\delta^{13}\text{C}_{\text{org}}$  values ranging from -30.67 to -41.26‰ (average  $-32.94 \pm 1.17\%$ ) reported here are  
4  
5 703 within the expected range for autotrophic carbon fixation (Schidlowski, 1988, 2001; Berg *et*  
6  
7 704 *al.*, 2010). The typical  $\delta^{13}\text{C}_{\text{org}}$  values generated by the widespread activity of ribulose 1,5-  
8  
9 705 bisphosphate carboxylase/oxygenase (RuBisCo), common in oxyphototrophic cyanobacteria  
10  
11 706 have average values from -20 to -30‰. These values are less negatively fractionated than  
12  
13 707 anoxygenic phototrophs (Quandt *et al.*, 1977; McNevin *et al.*, 2007; Berg *et al.*, 2010), while  
14  
15 708 more negative values  $<-30\%$  are related to autotrophic carbon fixation in the reductive acetyl  
16  
17 709 CoA pathway (*i.e.*, methanogenesis). In the case of the latter, acetoclastic methanogenesis  
18  
19 710 diagenetically supplies isotopically light  $^{12}\text{C}$  methane to anaerobic oxidation of methane  
20  
21 711 (AOM), the latter often comprising a consortia of sulfate reducers and methanotrophs (Conrad  
22  
23 712 *et al.*, 2010). Consequently, autotrophic carbon fixation via acetyl CoA pathway, combined  
24  
25 713 with anaerobic oxidation of fixed  $\text{C}_{\text{org}}$ , would effectively lead to deposition of residual  $\text{C}_{\text{org}}$   
26  
27 714 enriched in light  $^{12}\text{C}$  in the range found in this study. Such fixation of  $\text{CO}_2$  coupled with  
28  
29 715 diagenetic recycling of phototrophically derived  $\text{C}_{\text{org}}$  would have inevitably resulted in the  
30  
31 716 sequential overprinting of light  $\delta^{13}\text{C}$  in buried biomats. The bulk  $\delta^{13}\text{C}_{\text{org}}$  signatures  $<-30\%$   
32  
33 717 are, therefore, most parsimoniously interpreted to represent a mixed isotopic signal resulting  
34  
35 718 from the activities of various primary producers and heterotrophs.  
36  
37  
38

39  
40 719 The FB2b subunit hosts the first known multicellular organisms closely associated  
41  
42 720 with biomats (Figures 2, 10). Burrows, trails and resting traces of metazoans are often closely  
43  
44 721 associated with biomats in the past, being interpreted as sophisticated feeding behaviours (*e.g.*  
45  
46 722 Buatois & Mángano, 2012; Pecoits *et al.*, 2012; Buatois *et al.*, 2014; Meyer *et al.*, 2014; Chu  
47  
48 723 *et al.*, 2015). In modern environments, photosynthetic bacterial mats create thin  $\text{O}_2$ -rich  
49  
50 724 layers, thus providing benthic  $\text{O}_2$  oases for macroorganisms that may mine mat layers for  
51  
52 725 unexploited nutrients and  $\text{O}_2$  (Gingras *et al.*, 2011). It is perhaps not a coincidence then that  
53  
54 726 the biomats and macroorganisms belong to the same strata. Moreover, the generation of  
55  
56  
57  
58  
59  
60

1  
2  
3 727 microenvironments due to the chemical properties of EPS (Decho, 2000) may permit soft-  
4  
5 728 tissue mineralization, providing further protection against degradation (Sagemann *et al.*,  
6  
7 729 1999). Thus, the biomats may have stabilized the depositional surfaces and sheltered the  
8  
9 730 macroorganisms, allowing them to become imprinted into the rock record. Interestingly, the  
10  
11 731 large colonial organisms associated with bacterial communities are only known from the  
12  
13 732 FB2b rocks. Although other black shale facies are recorded in the Francevillian basin (*e.g.*,  
14  
15 733 the ~ 2.08 Ga FD black shale formation; Figure 1b), they were deposited in deeper  
16  
17 734 environments beyond the euphotic zone (Canfield *et al.*, 2013).  
18  
19  
20  
21

## 22 736 **Conclusion**

23  
24 737 Mat-related structures of the 2.1 Ga Francevillian series exhibit ten types of surface  
25  
26 738 morphologies, providing a new window into the highly diversified Paleoproterozoic microbial  
27  
28 739 life at that time. Mats are preserved in excellent conservation conditions from a 20 m thick  
29  
30 740 interval of sandstone and black shale facies.  
31  
32

33 741 Microtexture analyses provide strong evidence in favour of mat-colonized sediment. Oriented  
34  
35 742 grains, floating grains, heavy mineral concentrations, randomly oriented clays, pyritized  
36  
37 743 structures and wavy-crinkly laminae all reflect the growth of microbial communities.  
38  
39 744 Comparisons with ancient and modern analogues, as well as stable carbon isotope analyses,  
40  
41 745 suggest growth within a palaeoenvironmental settings corresponding to the euphotic zone,  
42  
43 746 likely less than 100m deep. Associations between Paleoproterozoic, large colonial organisms  
44  
45 747 and mats may be similar to interactions of Ediacaran early metazoans and microbial carpets  
46  
47 748 where O<sub>2</sub>-producing cyanobacterial mats may explain this specific pattern. In addition,  
48  
49 749 microbial mats may have played a major role in sediment biostabilization, fostering the  
50  
51 750 preservation of complex macroorganisms that represent the first ecosystem comprising  
52  
53 751 microbial biofilms and large colonial life forms.  
54  
55  
56  
57  
58  
59  
60

1  
2  
3 752  
4  
5 753  
6  
7 754  
8  
9 755  
10  
11 756  
12  
13 757  
14  
15 758  
16  
17 759  
18  
19 760  
20  
21 761  
22  
23 762  
24  
25 763  
26  
27 764  
28  
29 765  
30  
31 766  
32  
33 767  
34  
35 768  
36  
37 769  
38  
39 770  
40  
41 771  
42  
43 772  
44  
45 773  
46  
47 774  
48  
49 775  
50  
51 776  
52  
53  
54  
55  
56  
57  
58  
59  
60

## **Acknowledgements**

We thank the Ministry of Mines, Oil, Energy and Hydraulic Resources; General Direction of Mines and Geology of Gabon; Ministry of Education, Research and Culture; National Center for Scientific Research of Gabon (CENAREST); Sylvia Bongo Foundation; Agence Nationale des Parcs Nationaux of Gabon; University of Masuku; COMILOG-Company; French Embassy at Libreville; and Institut Français du Gabon, French Ministry for Foreign Affairs. ECF is funded by the European Research Council (ERC) Seventh Framework Program (FP7) grant No. 336092. Funding for KK and MG were provided by the Natural Sciences and Engineering Research Council (NSERC). For information and scientific discussion, we acknowledge O. Bankole, C. Fontaine and J-Y. Reynaud. For assistance, we thank N. Guignard (Raman microprobe analysis) and J. Laduranty (CHNS analysis). In France, we are grateful to the French CNRS, FEDER, the Universities of Poitiers and Lille 1, and the Nouvelle Aquitaine Region. All co-authors agree to the publication of this manuscript and declare no conflict of interest.



1  
2  
3 777  
4  
5 778  
6  
7 779  
8  
9 780  
10  
11 781  
12  
13 782  
14  
15 783  
16  
17 784  
18  
19 785  
20  
21 786  
22  
23 787  
24  
25 788  
26  
27 789  
28  
29 790  
30  
31 791

## References

- 32  
33  
34  
35 792 Azziley Azzibrouck G (1986) *Sédimentologie et géochimie du Francevillien B (Protérozoïque*  
36 793 *inférieur). Métallogénie des gisements de manganèse de Mouanda, Gabon.*
- 37  
38 794 Banerjee S, Jeevankumar S (2005) Microbially originated wrinkle structures on sandstone and their  
39 795 stratigraphic context: Palaeoproterozoic Koldaha Shale, central India. *Sedimentary Geology* **176**, 211–  
40 796 224.
- 41  
42 797 Banerjee S, Sarkar S, Eriksson PG, Hu X-F, Wang Y (2014) Palaeoenvironmental and biostratigraphic  
43 798 implications of microbial mat-related structures: Examples from the modern Gulf of Cambay and the  
44 799 Precambrian Vindhyan Basin, India. *Journal of Palaeogeography* **3**, 127–144.
- 45  
46 800 Banerjee S, Sarkar S, Eriksson PG, Samanta P (2010) Microbially related structures in siliciclastic  
47 801 sediment resembling Ediacaran fossils: examples from India, ancient and modern. In: *Microbial Mats:*  
48 802 *Modern and Ancient Microorganisms in Stratified Systems* (eds. Seckbach J, Oren A). Springer  
49 803 Netherlands, Dordrecht, pp. 109–129.
- 50  
51 804 Bankole OM, El Albani A, Meunier A, Rouxel OJ, Gauthier-Lafaye F, Bekker A (2016) Origin of red  
52 805 beds in the Paleoproterozoic Franceville Basin, Gabon, and implications for sandstone-hosted uranium  
53 806 mineralization. *American Journal of Science* **316**, 839–872.
- 54  
55 807 Bekker A, Holland HD (2012) Oxygen overshoot and recovery during the early Paleoproterozoic.  
56 808 *Earth and Planetary Science Letters* **317–318**, 295–304.
- 57  
58  
59  
60

- 1  
2  
3 809 Bekker A, Holland HD, Wang P-L, Rumble D, Stein HJ, Hannah JL, Coetzee LL, Beukes NJ (2004)  
4 810 Dating the rise of atmospheric oxygen. *Nature* **427**, 117–120.
- 5 811 Berg IA, Kockelkorn D, Ramos-Vera WH, Say RF, Zarzycki J, Hügler M, Alber BE, Fuchs G (2010)  
6 812 Autotrophic carbon fixation in archaea. *Nature Reviews Microbiology* **8**, 447–460.
- 7  
8 813 Berner RA (2004) *The Phanerozoic Carbon Cycle: CO<sub>2</sub> and O<sub>2</sub>*. Oxford University Press, Oxford.
- 9  
10 814 Bertrand-Sarfati J, Potin B (1994) Microfossiliferous cherty stromatolites in the 2000 Ma Franceville  
11 815 group, Gabon. *Precambrian research* **65**, 341–356.
- 12  
13 816 Bonhomme MG, Gauthier-Lafaye F, Weber F (1982) An example of Lower Proterozoic sediments:  
14 817 the Francevillian in Gabon. *Precambrian Research* **18**, 87–102.
- 15  
16 818 Bose S, Chafetz HS (2009) Topographic control on distribution of modern microbially induced  
17 819 sedimentary structures (MISS): A case study from Texas coast. *Sedimentary Geology* **213**, 136–149.
- 18  
19 820 Bottjer DJ, Hagadorn JW (2007) Mat-growth features. In: *Atlas of Microbial Mat Features Preserved*  
20 821 *within the Siliciclastic Rock Record* (eds. Schieber J, Bose PK, Eriksson PG, Banerjee S, Sarkar S,  
21 822 Altermann W, Catuneanu O). Elsevier, Amsterdam, pp. 53–71.
- 22  
23 823 Bouougri EH, Porada H (2007) Mat-related features from the terminal Ediacaran Nudaus Formation,  
24 824 Nama Group, Namibia. In: *Atlas of Microbial Mat Features Preserved within the Siliciclastic Rock*  
25 825 *Record* (eds. Schieber J, Bose PK, Eriksson PG, Banerjee S, Sarkar S, Altermann W, Catuneanu O).  
26 826 Elsevier, Amsterdam, pp. 214–222.
- 27  
28 827 Bouton P, Thiéblemont D, Gouin J, Cocherie A, Guerrot C, Tegye M, Prétat A, Simo Ndounze S,  
29 828 Kassadou AB, Boulingui B, Ekhogha H, Moussavou M (2009) Notice explicative de la Carte  
30 829 géologique de la République du Gabon à 1/200 000, feuille Franceville-Boumango, Libreville, 79p.
- 31  
32 830 Bros R, Stille P, Gauthier-Lafaye F, Weber F, Clauer N (1992) Sm-Nd isotopic dating of Proterozoic  
33 831 clay material: an example from the Francevillian sedimentary series, Gabon. *Earth and Planetary*  
34 832 *Science Letters* **113**, 207–218.
- 35  
36 833 Buatois LA, Mángano MG (2003) Early colonization of the deep sea: Ichnologic evidence of deep-  
37 834 marine benthic ecology from the Early Cambrian of northwest Argentina. *Palaios* **18**, 572–581.
- 38  
39 835 Buatois LA, Mángano MG (2012) The trace-fossil record of organism-matground interactions in space  
40 836 and time. In: *Microbial Mats in Siliclastic Depositional Systems Through Time* (eds. Noffke N,  
41 837 Chafetz H). SEPM (Society for Sedimentary Geology) Special Publication, Tulsa, Oklahoma, pp. 15–  
42 838 28.
- 43  
44 839 Buatois LA, Narbonne GM, Mángano MG, Carmona NB, Myrow P (2014) Ediacaran matground  
45 840 ecology persisted into the earliest Cambrian. *Nature Communications* **5**.
- 46  
47 841 Canfield DE, Ngombi-Pemba L, Hammarlund EU, Bengtson S, Chaussidon M, Gauthier-Lafaye F,  
48 842 Meunier A, Riboulleau A, Rollion-Bard C, Rouxel O, Asael D, Pierson-Wickmann A-C, El Albani A  
49 843 (2013) Oxygen dynamics in the aftermath of the Great Oxidation of Earth's atmosphere. *Proceedings*  
50 844 *of the National Academy of Sciences* **110**, 16736–16741.
- 51  
52 845 Chi Fru E, Arvestål E, Callac N, El Albani A, Kiliyas S, Argyraki A, Jakobsson M (2015) Arsenic  
53 846 stress after the Proterozoic glaciations. *Scientific Reports* **5**.
- 54  
55 847 Chu D, Tong J, Bottjer DJ, Song H, Song H, Benton MJ, Tian L, Guo W (2017) Microbial mats in the  
56 848 terrestrial Lower Triassic of North China and implications for the Permian–Triassic mass extinction.  
57 849 *Palaeogeography, Palaeoclimatology, Palaeoecology* **474**, 214–231.
- 58  
59  
60

- 1  
2  
3 850 Chu D, Tong J, Song H, Benton MJ, Bottjer DJ, Song H, Tian L (2015) Early Triassic wrinkle  
4 851 structures on land: stressed environments and oases for life. *Scientific Reports* **5**.
- 5 852 Conrad R, Claus P, Casper P (2010) Stable isotope fractionation during the methanogenic  
6 853 degradation of organic matter in the sediment of an acidic bog lake, Lake Grosse Fuchskuhle.  
7 854 *Limnology and Oceanography* **55**, 1932–1942.
- 8  
9 855 Davies NS, Liu AG, Gibling MR, Miller RF (2016) Resolving MISS conceptions and misconceptions:  
10 856 A geological approach to sedimentary surface textures generated by microbial and abiotic processes.  
11 857 *Earth-Science Reviews* **154**, 210–246.
- 12  
13 858 Decho AW (2000) Microbial biofilms in intertidal systems: an overview. *Continental Shelf Research*  
14 859 **20**, 1257–1273.
- 15  
16 860 Dubois M, Lopez M, Orberger B, Rodriguez C, Boussafir M, Dreux G, Rodrigues S, Pambo F (2015)  
17 861 The Mn-Carbonate Rich Black Shales of the Bangombe Plateau, Francevillian Basin, Gabon. In:  
18 862 *Mineral Ressources in a Sustainable World* (eds. André-Mayer AS, Cathelineau M, Muchez P, Pirard  
19 863 E, Sindern S). Presented at the Proceedings of the 13th Biennial SGA Meeting, Nancy, France, pp.  
20 864 1905–1908.
- 21  
22 865 El Albani A, Bengtson S, Canfield DE, Riboulleau A, Rollion Bard C, Macchiarelli R, Ngombi Pemba  
23 866 L, Hammarlund E, Meunier A, Moubiya Mouele I, Benzerara K, Bernard S, Boulvais P, Chaussidon  
24 867 M, Cesari C, Fontaine C, Chi-Fru E, Garcia Ruiz JM, Gauthier-Lafaye F, Mazurier A, Pierson-  
25 868 Wickmann AC, Rouxel O, Trentesaux A, Vecoli M, Versteegh GJM, White L, Whitehouse M, Bekker  
26 869 A (2014) The 2.1 Ga Old Francevillian Biota: Biogenicity, Taphonomy and Biodiversity. *PLoS ONE*  
27 870 **9**, e99438.
- 28  
29 871 El Albani AE, Bengtson S, Canfield DE, Bekker A, Macchiarelli R, Mazurier A, Hammarlund EU,  
30 872 Boulvais P, Dupuy J-J, Fontaine C, Fürsich FT, Gauthier-Lafaye F, Janvier P, Javaux E, Ossa FO,  
31 873 Pierson-Wickmann A-C, Riboulleau A, Sardini P, Vachard D, Whitehouse M, Meunier A (2010)  
32 874 Large colonial organisms with coordinated growth in oxygenated environments 2.1 Gyr ago. *Nature*  
33 875 **466**, 100–104.
- 34  
35 876 Eriksson PG, Sarkar S, Samanta P, Banerjee S, Porada H, Catuneanu O (2010) Paleoenvironmental  
36 877 Context of Microbial Mat-Related Structures in Siliciclastic Rocks. In: *Microbial Mats: Modern and*  
37 878 *Ancient Microorganisms in Stratified Systems* (eds. Seckbach J, Oren A). Springer Netherlands,  
38 879 Dordrecht, pp. 71–108.
- 39  
40 880 Farquhar J, Zerkle AL, Bekker A (2011) Geological constraints on the origin of oxygenic  
41 881 photosynthesis. *Photosynthesis Research* **107**, 11–36.
- 42  
43 882 Flannery DT, Walter MR (2012) Archean tufted microbial mats and the Great Oxidation Event: new  
44 883 insights into an ancient problem. *Australian Journal of Earth Sciences* **59**, 1–11.
- 45  
46 884 Flood BE, Bailey JV, Biddle JF (2014) Horizontal gene transfer and the rock record: comparative  
47 885 genomics of phylogenetically distant bacteria that induce wrinkle structure formation in modern  
48 886 sediments. *Geobiology* **12**, 119–132.
- 49  
50 887 Gancarz AJ (1978) U-Pb age ( $2.05 \times 10^9$  years) of the Oklo uranium deposit. Presented at the The  
51 888 Natural Fission Reactors: Annual International Atomic Energy Agency Conference, Vienna, Austria,  
52 889 pp. 513–520.
- 53  
54 890 Garlick WG (1988) Algal Mats, Load Structures, and Synsedimentary Sulfides in Revett Quartzites of  
55 891 Montana and Idaho. *Economic Geology* **83**, 1259–1278.
- 56  
57 892 Gauthier-Lafaye F (2006) Time constraint for the occurrence of uranium deposits and natural nuclear  
58  
59  
60

- 1  
2  
3 893 fission reactors in the Paleoproterozoic Franceville Basin (Gabon). *Geological Society of America*  
4 894 *Memoirs* **198**, 157–167.
- 5 895 Gauthier-Lafaye F, Weber F (1989) The Francevillian (Lower Proterozoic) Uranium Ore Deposits of  
6 896 Gabon. *Economic Geology* **84**, 2267–2285.
- 7  
8 897 Gauthier-Lafaye F, Weber F (2003) Natural nuclear fission reactors: time constraints for occurrence,  
9 898 and their relation to uranium and manganese deposits and to the evolution of the atmosphere.  
10 899 *Precambrian Research* **120**, 81–100.
- 11  
12 900 Gehling JG (1999) Microbial mats in terminal Proterozoic siliciclastics; Ediacaran death masks.  
13 901 *Palaios* **14**, 40–57.
- 14  
15 902 Gerdes G (2007) Structures left by modern microbial mats in their host sediments. In: *Atlas of*  
16 903 *Microbial Mat Features Preserved within the Siliciclastic Rock Record* (eds. Schieber J, Bose PK,  
17 904 Eriksson PG, Banerjee S, Sarkar S, Altermann W, Catuneanu O). Elsevier, Amsterdam, pp. 5–38.
- 18  
19 905 Gerdes G, Claes M, Dunajtschik-Piewak K, Riege H, Krumbein WE, Reineck H-E (1993)  
20 906 Contribution of microbial mats to sedimentary surface structures. *Facies* **29**, 61.
- 21  
22 907 Gerdes G, Klenke T, Noffke N (2000) Microbial signatures in peritidal siliciclastic sediments: a  
23 908 catalogue. *Sedimentology* **47**, 279–308.
- 24  
25 909 Gerdes G, Krumbein WE, Reineck H-E (1994) Microbial mats as architects of sedimentary surface  
26 910 structures. In: *Biostabilization of Sediments* (eds. Krumbein WE, Paterson DM, Stal LJ). Bibliotheks  
27 911 und Informationssystem der Carl von Ossietzky Universität Oldenburg (BIS)-Verlag, Oldenburg, pp.  
28 912 165–182.
- 29  
30 913 Gingras M, Hagadorn JW, Seilacher A, Lalonde SV, Pecoits E, Petrash D, Konhauser KO (2011)  
31 914 Possible evolution of mobile animals in association with microbial mats. *Nature Geoscience* **4**, 372–  
32 915 375.
- 33  
34 916 Grazhdankin D, Gerdes G (2007) Ediacaran microbial colonies: Ediacaran microbial colonies. *Lethaia*  
35 917 **40**, 201–210.
- 36  
37 918 Hagadorn JW, Bottjer DJ (1997) Wrinkle structures: Microbially mediated sedimentary structures  
38 919 common in subtidal siliciclastic settings at the Proterozoic-Phanerozoic transition. *Geology* **25**, 1047.
- 39  
40 920 Hill C, Corcoran PL, Aranha R, Longstaffe FJ (2016) Microbially induced sedimentary structures in  
41 921 the Paleoproterozoic, upper Huronian Supergroup, Canada. *Precambrian Research* **281**, 155–165.
- 42  
43 922 Holland HD (2002) Volcanic gases, black smokers, and the Great Oxidation Event. *Geochimica et*  
44 923 *Cosmochimica Acta* **66**, 3811–3826.
- 45  
46 924 Homann M, Heubeck C, Airo A, Tice MM (2015) Morphological adaptations of 3.22 Ga-old tufted  
47 925 microbial mats to Archean coastal habitats (Moodies Group, Barberton Greenstone Belt, South  
48 926 Africa). *Precambrian Research* **266**, 47–64.
- 49  
50 927 Horie K, Hidaka H, Gauthier-Lafaye F (2005) U-Pb geochronology and geochemistry of zircon from  
51 928 the Franceville series at Bidoudouma, Gabon. Presented at the The 15th Annual Goldschmidt  
52 929 Conference, Moscow, United States.
- 53  
54 930 Immenhauser A (2009) Estimating palaeo-water depth from the physical rock record. *Earth-Science*  
55 931 *Reviews* **96**, 107–139.
- 56  
57 932 Jungblut AD, Hawes I, Mackey TJ, Krusor M, Doran PT, Sumner DY, Eisen JA, Hillman C, Goroncy  
58 933 AK (2016) Microbial Mat Communities along an Oxygen Gradient in a Perennially Ice-Covered

- 1  
2  
3 934 Antarctic Lake. *Applied and Environmental Microbiology* **82**, 620–630.
- 4 935 Karhu JA, Holland HD (1996) Carbon isotopes and the rise of atmospheric oxygen. *Geology* **24**, 867–  
5 936 870.
- 6  
7 937 Konhauser KO, Lalonde SV, Planavsky NJ, Pecoits E, Lyons TW, Mojzsis SJ, Rouxel OJ, Barley ME,  
8 938 Rosiere C, Fralick PW, Kump LR, Bekker A (2011) Aerobic bacterial pyrite oxidation and acid rock  
9 939 drainage during the Great Oxidation Event. *Nature* **478**, 369–373.
- 10  
11 940 Kovalchuk O, Owttrim GW, Konhauser KO, Gingras MK (2017) Desiccation cracks in siliciclastic  
12 941 deposits: Microbial mat-related compared to abiotic sedimentary origin. *Sedimentary Geology* **347**,  
13 942 67–78.
- 14  
15 943 Lekele Baghekema SG, Lepot K, Riboulleau A, Fadel A, Trentesaux A, El Albani A (2017) Nanoscale  
16 944 analysis of preservation of ca. 2.1 Ga old Francevillian microfossils, Gabon. *Precambrian Research*  
17 945 **301**, 1–18.
- 18  
19 946 Lyons TW, Reinhard CT, Planavsky NJ (2014) The rise of oxygen in Earth's early ocean and  
20 947 atmosphere. *Nature* **506**, 307–315.
- 21 948 Mariotti G, Pruss SB, Perron JT, Bosak T (2014) Microbial shaping of sedimentary wrinkle structures.  
22 949 *Nature Geoscience* **7**, 736–740.
- 23  
24 950 Mata SA, Bottjer DJ (2009) The paleoenvironmental distribution of Phanerozoic wrinkle structures.  
25 951 *Earth-Science Reviews* **96**, 181–195.
- 26  
27 952 Matsushita M, Hiramatsu F, Kobayashi N, Ozawa T, Yamazaki Y, Matsuyama T (2004) Colony  
28 953 formation in bacteria: experiments and modeling. *Biofilms* **1**, 305–317.
- 29  
30 954 McNevin DB, Badger MR, Whitney SM, Caemmerer GG von, Tcherkez GG, Farquhar GD (2007)  
31 955 Differences in carbon isotope discrimination of three variants of D-ribulose-1,5-bisphosphate  
32 956 carboxylase/oxygenase reflect differences in their catalytic mechanisms. *Journal of Biological*  
33 957 *Chemistry* **282**, 36068–36076.
- 34  
35 958 Meyer M, Xiao S, Gill BC, Schiffbauer JD, Chen Z, Zhou C, Yuan X (2014) Interactions between  
36 959 Ediacaran animals and microbial mats: Insights from Lamonte trevallis, a new trace fossil from the  
37 960 Dengying Formation of South China. *Palaeogeography, Palaeoclimatology, Palaeoecology* **396**, 62–  
38 961 74.
- 39  
40 962 Mouélé IM, Dudoignon P, El Albani A, Meunier A, Boulvais P, Gauthier-Lafaye F, Paquette J-L,  
41 963 Martin H, Cuney M (2014) 2.9–1.9 Ga paleoalterations of Archean granitic basement of the  
42 964 Franceville basin (Gabon). *Journal of African Earth Sciences* **97**, 244–260.
- 43  
44 965 Ngombi Pemba L (2014) *Géochimie et minéralogie des formations argileuses (2.2 – 2.0 Ga) du bassin*  
45 966 *de Franceville au Gabon : fluctuations de l'oxygène atmosphérique, chimie des océans et diagenèse*  
46 967 *au Paléoprotérozoïque*.
- 47  
48 968 Ngombi-Pemba L, Albani AE, Meunier A, Grauby O, Gauthier-Lafaye F (2014) From detrital heritage  
49 969 to diagenetic transformations, the message of clay minerals contained within shales of the  
50 970 Palaeoproterozoic Francevillian basin (Gabon). *Precambrian Research* **255**, 63–76.
- 51 971 Noffke N (2009) The criteria for the biogenicity of microbially induced sedimentary structures  
52 972 (MISS) in Archean and younger, sandy deposits. *Earth-Science Reviews* **96**, 173–180.
- 53  
54 973 Noffke N (2010) *Geobiology*. Springer Berlin Heidelberg, Berlin, Heidelberg.
- 55  
56 974 Noffke N, Christian D, Wacey D, Hazen RM (2013) Microbially Induced Sedimentary Structures

- 1  
2  
3 975 Recording an Ancient Ecosystem in the *ca.* 3.48 Billion-Year-Old Dresser Formation, Pilbara,  
4 976 Western Australia. *Astrobiology* **13**, 1103–1124.
- 5 977 Noffke N, Gerdes G, Klenke T, Krumbein WE (1997) A microscopic sedimentary succession of  
6 978 graded sand and microbial mats in modern siliciclastic tidal flats. *Sedimentary Geology* **110**, 1–6.
- 8 979 Noffke N, Gerdes G, Klenke T, Krumbein WE (2001) Microbially Induced Sedimentary Structures—A  
9 980 New Category within the Classification of Primary Sedimentary Structures: PERSPECTIVES. *Journal*  
10 981 *of Sedimentary Research* **71**, 649–656.
- 12 982 Noffke N, Knoll AH, Grotzinger JP (2002) Sedimentary controls on the formation and preservation of  
13 983 microbial mats in siliciclastic deposits: a case study from the Upper Neoproterozoic Nama Group,  
14 984 Namibia. *Palaios* **17**, 533–544.
- 16 985 Ossa Ossa F-G (2010) *Etude multi-approches du bassin sédimentaire paléoprotérozoïque (2. 1-2. 4*  
17 986 *Ga) de Franceville au Gabon: les environnements sédimentaires et l'impact des paléocirculations de*  
18 987 *fluides.*
- 19 988 Parize O, Feybesse J-L, Guillocheau F, Mulder T (2013) Were the 2.1-Gyr fossil colonial organisms  
20 989 discovered in the Francevillian basin (Palaeoproterozoic, Gabon) buried by turbidites? *Comptes*  
21 990 *Rendus Geoscience* **345**, 101–110.
- 23 991 Partin CA, Lalonde SV, Planavsky NJ, Bekker A, Rouxel OJ, Lyons TW, Konhauser KO (2013a)  
24 992 Uranium in iron formations and the rise of atmospheric oxygen. *Chemical Geology* **362**, 82–90.
- 26 993 Partin CA, Bekker A, Planavsky NJ, Scott CT, Gill BC, Li C, Podkovyrov V, Maslov A, Konhauser  
27 994 KO, Lalonde SV, Love GD, Poulton SW, Lyons TW (2013b) Large-scale fluctuations in Precambrian  
28 995 atmospheric and oceanic oxygen levels from the record of U in shales. *Earth and Planetary Science*  
29 996 *Letters* **369–370**, 284–293.
- 31 997 Pecoits E, Konhauser KO, Aubert NR, Heaman LM, Veroslavsky G, Stern RA, Gingras MK (2012)  
32 998 Bilaterian Burrows and Grazing Behavior at >585 Million Years Ago. *Science* **336**, 1693–1696.
- 34 999 Pfluger F (1999) Matground Structures and Redox Facies. *PALAIOS* **14**, 25.
- 36 1000 Porada H, Bouougri EH (2007) Wrinkle structures—a critical review. In: *Atlas of Microbial Mat*  
37 1001 *Features Preserved within the Siliciclastic Rock Record* (eds. Schieber J, Bose PK, Eriksson PG,  
38 1002 Banerjee S, Sarkar S, Altermann W, Catuneanu O). Elsevier, Amsterdam, pp. 135–144.
- 39 1003 Porada H, Bouougri EH, Ghergut J (2007) Hydraulic conditions and mat-related structures in tidal  
40 1004 flats and coastal sabkhas. In: *Atlas of Microbial Mat Features Preserved within the Siliciclastic Rock*  
41 1005 *Record* (eds. Schieber J, Bose PK, Eriksson PG, Banerjee S, Sarkar S, Altermann W, Catuneanu O).  
42 1006 Elsevier, Amsterdam, pp. 258–265.
- 44 1007 Porada H, Ghergut J, Bouougri EH (2008) Kinneyia-type wrinkle structures - Critical review and  
45 1008 model of formation. *PALAIOS* **23**, 65–77.
- 47 1009 Quandt L, Gottschalk G, Ziegler H, Stichler W (1977) Isotope discrimination by photosynthetic  
48 1010 bacteria. *FEMS Microbiology Letters* **1**, 125–128.
- 50 1011 Reineck H-E, Singh IB (1980) *Depositional Sedimentary Environments*. Springer Berlin Heidelberg,  
51 1012 Berlin, Heidelberg.
- 52 1013 Reyes K, Gonzalez NI, Stewart J, Ospino F, Nguyen D, Cho DT, Ghahremani N, Spear JR, Johnson  
53 1014 HA (2013) Surface Orientation Affects the Direction of Cone Growth by *Leptolyngbya* sp. Strain C1,  
54 1015 a Likely Architect of Coniform Structures Octopus Spring (Yellowstone National Park). *Applied and*  
55 1016 *Environmental Microbiology* **79**, 1302–1308.

- 1  
2  
3 1017 Reynaud J-Y, Trentesaux A, El Albani A, Aubineau J, Ngombi-Pemba L, Guiyeligou G, Bouton P,  
4 1018 Gauthier-Lafaye F, Weber F (2017) Depositional setting of the 2.1 Ga Francevillian macrobiota  
5 1019 (Gabon): Rapid mud settling in a shallow basin swept by high-density sand flows. *Sedimentology*.  
6  
7 1020 Runnegar BN, Fedonkin MA (1992) Proterozoic Metazoan Body Fossils. In: *The Proterozoic*  
8 1021 *Biosphere: A Multidisciplinary Study* (eds. Schopf JW, Klein C). Cambridge University Press,  
9 1022 Cambridge, pp. 369–388.  
10  
11 1023 Sagemann J, Bale SJ, Briggs DE, Parkes RJ (1999) Controls on the formation of authigenic minerals  
12 1024 in association with decaying organic matter: an experimental approach. *Geochimica et Cosmochimica*  
13 1025 *Acta* **63**, 1083–1095.  
14  
15 1026 Sarkar S, Banerjee S, Samanta P, Chakraborty N, Chakraborty PP, Mukhopadhyay S, Singh AK  
16 1027 (2014) Microbial mat records in siliciclastic rocks: Examples from Four Indian Proterozoic basins and  
17 1028 their modern equivalents in Gulf of Cambay. *Journal of Asian Earth Sciences* **91**, 362–377.  
18  
19 1029 Sarkar S, Banerjee S, Samanta P, Jeevankumar S (2006) Microbial mat-induced sedimentary  
20 1030 structures in siliciclastic sediments: examples from the 1.6 Ga Chorhat Sandstone, Vindhyan  
21 1031 Supergroup, MP, India. *Journal of Earth System Science* **115**, 49–60.  
22  
23 1032 Sarkar S, Bose P, Samanta P, Sengupta P, Eriksson P (2008) Microbial mat mediated structures in the  
24 1033 Ediacaran Sonia Sandstone, Rajasthan, India, and their implications for Proterozoic sedimentation.  
25 1034 *Precambrian Research* **162**, 248–263.  
26  
27 1035 Sarkar S, Choudhuri A, Mandal S, Eriksson PG (2016) Microbial mat-related structures shared by  
28 1036 both siliciclastic and carbonate formations. *Journal of Palaeogeography* **5**, 278–291.  
29  
30 1037 Schidlowski M (1988) A 3,800-million-year isotopic record of life from carbon in sedimentary rocks.  
31 1038 *Nature* **333**, 313–318.  
32  
33 1039 Schidlowski M (2001) Carbon isotopes as biogeochemical recorders of life over 3.8 Ga of Earth  
34 1040 history: evolution of a concept. *Precambrian Research* **106**, 117–134.  
35  
36 1041 Schieber J (1998) Possible indicators of microbial mat deposits in shales and sandstones: examples  
37 1042 from the Mid-Proterozoic Belt Supergroup, Montana, U.S.A. *Sedimentary Geology* **120**, 105–124.  
38  
39 1043 Schieber J (1999) Microbial mats in terrigenous clastics; the challenge of identification in the rock  
40 1044 record. *Palaios* **14**, 3–12.  
41  
42 1045 Schwark L, Frimmel A (2004) Chemostratigraphy of the Posidonia Black Shale, SW-Germany II.  
43 1046 Assessment of extent and persistence of photic-zone anoxia using aryl isoprenoid distributions.  
44 1047 *Chemical Geology* **206**, 231–248.  
45  
46 1048 Sheldon ND (2012) Microbially Induced Sedimentary Structures in the Ca. 1100 Ma Terrestrial  
47 1049 Midcontinent Rift of North America. In: *Microbial Mats in Siliclastic Depositional Systems Through*  
48 1050 *Time* (eds. Noffke N, Chafetz HS). SEPM (Society for Sedimentary Geology) Special Publication,  
49 1051 Tulsa, Oklahoma, pp. 153–162.  
50  
51 1052 Shepard RN, Sumner DY (2010) Undirected motility of filamentous cyanobacteria produces reticulate  
52 1053 mats: Motility produces reticulate mats. *Geobiology* **8**, 179–190.  
53  
54 1054 Sim MS, Liang B, Petroff AP, Evans A, Klepac-Ceraj V, Flannery DT, Walter MR, Bosak T (2012)  
55 1055 Oxygen-Dependent Morphogenesis of Modern Clumped Photosynthetic Mats and Implications for the  
56 1056 Archean Stromatolite Record. *Geosciences* **2**, 235–259.  
57  
58 1057 Simpson EL, Heness E, Bumby A, Eriksson PG, Eriksson KA, Hilbert-Wolf HL, Linnevelt S,  
59 1058 Malenda HF, Modungwa T, Okafor OJ (2013) Evidence for 2.0 Ga continental microbial mats in a  
60

- 1059 paleodesert setting. *Precambrian Research* **237**, 36–50.
- 1060 Sumner DY, Hawes I, Mackey TJ, Jungblut AD, Doran PT (2015) Antarctic microbial mats: A  
1061 modern analog for Archean lacustrine oxygen oases. *Geology* **43**, 887–890.
- 1062 Taj RJ, Aref MAM, Schreiber BC (2014) The influence of microbial mats on the formation of sand  
1063 volcanoes and mounds in the Red Sea coastal plain, south Jeddah, Saudi Arabia. *Sedimentary Geology*  
1064 **311**, 60–74.
- 1065 Thomas K, Herminghaus S, Porada H, Goehring L (2013) Formation of Kinneyia via shear-induced  
1066 instabilities in microbial mats. *Philosophical Transactions of the Royal Society A: Mathematical,*  
1067 *Physical and Engineering Sciences* **371**, 20120362–20120362.
- 1068 Velde BD, Meunier A (2008) *The Origin of Clay Minerals in Soils and Weathered Rocks*. Springer-  
1069 Verlag, Berlin.
- 1070 Wacey D (2009) *Early life on earth: a practical guide*. Topics in geobiology. Springer, Dordrecht.
- 1071 Walcott CD (1914) Cambrian Geology and Palaeontology III, No. 2. Precambrian, Algonkian algal  
1072 flora. *Smithsonian Miscellaneous Collections* **64**, 77–156.
- 1073 Weber F (1969) *Une série précambrienne du Gabon : le Francevillien. Sédimentologie, géochimie,*  
1074 *relations avec les gîtes minéraux associés*.
- 1075 Wilmeth DT, Dornbos SQ, Isbell JL, Czaja AD (2014) Putative domal microbial structures in fluvial  
1076 siliciclastic facies of the Mesoproterozoic (1.09 Ga) Copper Harbor Conglomerate, Upper Peninsula of  
1077 Michigan, USA. *Geobiology* **12**, 99–108.
- 1078 Yang H, Chen Z-Q, Fang Y (2017) Microbially induced sedimentary structures from the 1.64 Ga  
1079 Chuanlinggou Formation, Jixian, North China. *Palaeogeography, Palaeoclimatology, Palaeoecology*  
1080 **474**, 7–25.

1081

1082 **Figure captions**

1083 **FIGURE 1 Geological map and lithostratigraphic column.** (a) Geological map of the Francevillian basin. The  
1084 studied quarry is Moulendé (green star). Geological map adopted from (Bouton *et al.*, 2009). (b) Synthetic  
1085 lithostratigraphy of the Francevillian series. Four sedimentary units rest unconformably on Archean rocks. The  
1086 red star indicates the detailed lithostratigraphic column observed in the Moulendé quarry (Figure 2).

1087 **FIGURE 2 Detailed lithostratigraphic column.** Composite columnar section of the Moulendé quarry in the  
1088 FB2 unit showing the vertical distribution of ten representative types of mat-related structures (MRS) and  
1089 sedimentary structures (SS).

1090 **FIGURE 3 Plane view and outcrop pictures of sedimentary facies in the Moulendé quarry.** (a)  
1091 Representation of the quarry from plane view. Red box indicates the main studied outcrop in B (F8). F =  
1092 outcrops. (b) Details of the bedding geometry at the transition between massive sandstone beds and thinly  
1093 laminated black shales. (c) Closer view of B. (d) Cross-section view of decimetre-scale hummocky-cross  
1094 stratifications (HCS), FB2a subunit. (e) Sandstone dyke, FB2a - FB2b transition. Coin diameter: ~ 2 cm. (f)  
1095 Cross-section view of convolute structures, FB2b subunit. (g) Bedding plane view of interference ripples, FB2b  
1096 subunit. (h) Longitudinal view of dark-coloured convex laminae associated with cm-scale foreset beds, FB2b  
1097 subunit.



1  
2  
3 1098 **FIGURE 4 Microbial mat structures in the Francevillian B Formation (FB2): Mat-layer structures.** (a-c)  
4 1099 ‘Elephant-skin’ textures. (d) Putative macro-tufted microbial mat. (e-f) Clustered domal buildups and flat  
5 1100 pyritized microbial structure (red arrow). Macrofossil specimens (white arrows). (g) Isolated domal buildups. (h)  
6 1101 Wrinkle marks.

8  
9 1102 **FIGURE 5 Microbial mat structures in the Francevillian B Formation (FB2): Mat-layer structures.** (a-b)  
10 1103 Discoidal mats likely representing ‘fairy ring’ structures. (c-e) Disc-shaped mats that display a cauliflower-like  
11 1104 pattern. (f) Disc-shaped mat with internal wrinkle structures. (g) Small pyritized circular bodies. (h) Horizontal  
12 1105 mat growth pattern.

14  
15 1106 **FIGURE 6 Mat-related structures in the Francevillian B Formation (FB2): Mat-protected structures.** (a-b)  
16 1107 Parallel wavy wrinkle structures. (c) Cross-cutting wrinkle structures. (d) ‘Kinneyia’ structure. (e) Linear pattern.  
17 1108 Dashed red box indicates the position of the magnification in f. Red arrow shows the location where the  
18 1109 spectrometry Raman was performed. The Raman spectra is visible in Figure 8d. (f) Micrometric spots  
19 1110 interpreting as oriented grains. (g) Linear patterns with several parallel ridges. (h) Nodular-like structure.

21  
22 1111 **FIGURE 7 Optical photomicrographs of mat-related structures.** (a) Transmitted thin section of ‘elephant-  
23 1112 skin’ texture. Dashed red box denoting area magnified in f. (b) Transmitted thin section of putative macro-tufted  
24 1113 microbial mat. Dashed red boxes denoting areas magnified in g and h. (c) Transmitted thin section of an isolated  
25 1114 domal buildup. Dashed red box denoting area magnified in i. (d) Transmitted thin section of parallel wavy  
26 1115 wrinkle structures. Dashed red box denoting area magnified in j. (e) Transmitted thin section of a linear pattern.  
27 1116 Dashed red boxes denoting areas magnified in k and Figure 9e. (f) Tufted microstructures and wavy-crinkly  
28 1117 laminae. Dashed red box denoting area magnified in Figure 9a. (g-h) Thickness variation across the mat layer  
29 1118 with floating grains embedded by clays (red arrows). Mica (white arrows). Dashed red box denoting area  
30 1119 magnified in Figure 9c. (i) Reflected magnified thin section of an entirely pyritized dome. An internal convex  
31 1120 lamination is indicated by dashed red lines. (j) Clay laminae do not onlap the rippled siltstone bed but rather well  
32 1121 follow its topography. Oriented grains (arrows). (k) High amount of quartz particles (arrows as example) within  
33 1122 dark-coloured laminae. Dashed red box denoting area magnified in Figure 9d.

35  
36  
37  
38  
39 1123 **FIGURE 8 Polished slab of ‘elephant-skin’ texture and Raman spectra of both ‘elephant-skin’ texture and**  
40 1124 **linear pattern.** (a) Polished slab in cross-section perpendicular to bedding plane. Non-homogenous dark layer  
41 1125 preserved above a pronounced boundary. Red arrow and white arrow indicate Raman spectra in b and c,  
42 1126 respectively. (b) Representative Raman spectra of the microbial mat within bulges. It shows the presence of two  
43 1127 Carbon peaks (“C”) at  $1336\text{ cm}^{-1}$  (the “D1” disordered peak) and  $1603\text{ cm}^{-1}$  (the “G” graphite peak). (c) Typical  
44 1128 Raman spectra of sandstone with quartz (“Q”) peaks. (d) Representative Raman spectra of mat layers of linear  
45 1129 pattern indicated in Figure 6e. It shows the presence of three carbon peaks (“C”) at  $\sim 1170\text{ cm}^{-1}$  (“D4” disordered  
46 1130 peak),  $1344\text{ cm}^{-1}$  (the “D1” disordered peak) and  $1603\text{ cm}^{-1}$  (the “G” graphite peak). (e) Typical Raman spectra  
47 1131 of host sediment of linear pattern, with quartz (Q) peaks and very small intensities of “C” peaks.

51  
52 1132 **FIGURE 9 SEM imaging of mat-related structures.** (a) Magnified view of box area in Figure 7f. Upward clay  
53 1133 laminae within tufted microstructures and wavy-crinkly layers. (b). Tufted microstructures and heavy minerals  
54 1134 constitute bulges of the ‘elephant-skin’ texture. (c) Magnified view of box area in Figure 7h. Quartz grains,  
55 1135 heavy minerals and randomly oriented clays constitute the dark-coloured mat layer. (d) Magnified view of box

1  
2  
3 1136 area in Figure 7k. Detrital particles wrapped by sheet clays. (e) Magnified view of box area in Figure 7e. Clay  
4 1137 minerals above and throughout the ridge (arrow). No significant clue of liquefaction nor microbial shrinkage.

5  
6 1138 **FIGURE 10 Examples of fossil macroorganisms associated with microbial mats.** (a) Pyritized lobate form  
7 1139 just beneath ‘fairy ring’ structures. (b) Disk with radially striated core (arrow) lies on domal buildups. (c-d) Disk  
8 1140 or lobate form and flat pyritized microbial structures on the same strata are closely associated. (e) Circular disks  
9 1141 (arrows) rest on wrinkle marks. (f) Disk and lobate form are close to wrinkle marks on the same level or not.

11 1142

13 1143

15 1144

17 1145

19 1146

21 1147

23 1148

25 1149

27 1150

29 1151

31 1152

33 1153 **Captions for the supplementary information**

35 1154 **FIGURE S1 Additional flat pyritized microbial mats.**

37 1155 **FIGURE S2 EDS elemental maps of bulges of reticulate patterns in cross-section perpendicular to**  
38 1156 **bedding plane.** BSE and composite elemental maps. Note the wavy-crinkly laminae with a large amount of  
39 1157 embedded heavy minerals.

41  
42 1158 **FIGURE S3 Photographs of mat-layer structures found in literature.** (a) Analogous ‘elephant-skin’ texture  
43 1159 from modern lower supratidal, Bahar Alouane, southern Tunisia. Modified after photo published in Gerdes  
44 1160 (2007). (b) Fossil reticulate pattern on bedding plane of siliciclastic beds from the Archean Tumbiana  
45 1161 Formation, Australia. Modified after photo published in Flannery & Walter (2012). (c) A 2.0 billion-years-old  
46 1162 tufted microbial mat from Makgabeng Formation, South Africa. Modified after photo published in Simpson *et*  
47 1163 *al.* (2013). (d) Analogue clustered low mound-like structures with *Protichnites* trackways on bedding surface of  
48 1164 quartz arenites from the Late Cambrian, Elk Mound Group, USA. Modified after photo published in Bottjer &  
49 1165 Hagadorn (2007). (e) Modern analogous ‘fairy rings’ on soft muddy sediments from Bretagne salterns, France.  
50 1166 Modified after photo published in Grazhdankin & Gerdes (2007). (f) Ancient example of outward-convex,  
51 1167 spindle-shaped discoidal structures with concentric rings from the Mesoproterozoic, Sonia Sandstone, India.  
52 1168 Modified after photo published in Sarkar *et al.* (2014). (g) Modern discoidal microbial colony on tidal flat from

1  
2  
3 1169 the Gulf of Cambay, India. Modified after photo published in Banerjee *et al.* (2014). Lens cap diameter: 6 cm.  
4 1170 (h) Analogue discoidal microbial colony on bedding plane of sandstones from the Precambrian Vindhyan  
5 1171 Supergroup, India. Modified after photo published in Banerjee *et al.* (2014).  
6

7 1172 **FIGURE S4 Photographs of mat-related structures found in literature.** (a) Modern example of submerged  
8 1173 wrinkle marks from Redfish Bay, Texas. Modified after photo published in Hagadorn & Bottjer (1997). (b)  
9 1174 Patches of wrinkle marks on bedding surface of fine-grained sandstones from the Early Cambrian, Chapel Island  
10 1175 Formation, Canada. Modified after photo published in Buatois *et al.* (2014). (c) Parallel wavy wrinkle structures  
11 1176 reproduced in wave tank experiments using microbial aggregates. Modified after photo published in Mariotti *et*  
12 1177 *al.* (2014). (d) Analogous parallel wavy wrinkle structures on bedding plane of mudstones from the Early  
13 1178 Cambrian, Northwest Argentina. Modified after photo published in Buatois & Mángano (2003). (e) Minute  
14 1179 “Kinneyia” structures formed with microbial aggregates in wave tank experiments. Modified after photo  
15 1180 published in Mariotti *et al.* (2014). (f) Ancient analogue “Kinneyia” structures on bedding surface of siltstones  
16 1181 from the Cambrian, Oeland, Sweden. Modified after photo published in Porada & Bouougri (2007). (g) Linear  
17 1182 features from modern tidal flats of Bhar Alouane, southern Tunisia. Modified after photo published in Porada &  
18 1183 Bouougri (2007). (h) Putative linear patterns on bedding surface of fine-grained quartzites from the  
19 1184 Neoproterozoic Katanga Supergroup, Zambia. Modified after photo published in Porada & Bouougri (2007).  
20  
21  
22  
23  
24  
25  
26  
27  
28  
29  
30  
31  
32  
33  
34  
35  
36  
37  
38  
39  
40  
41  
42  
43  
44  
45  
46  
47  
48  
49  
50  
51  
52  
53  
54  
55  
56  
57  
58  
59  
60

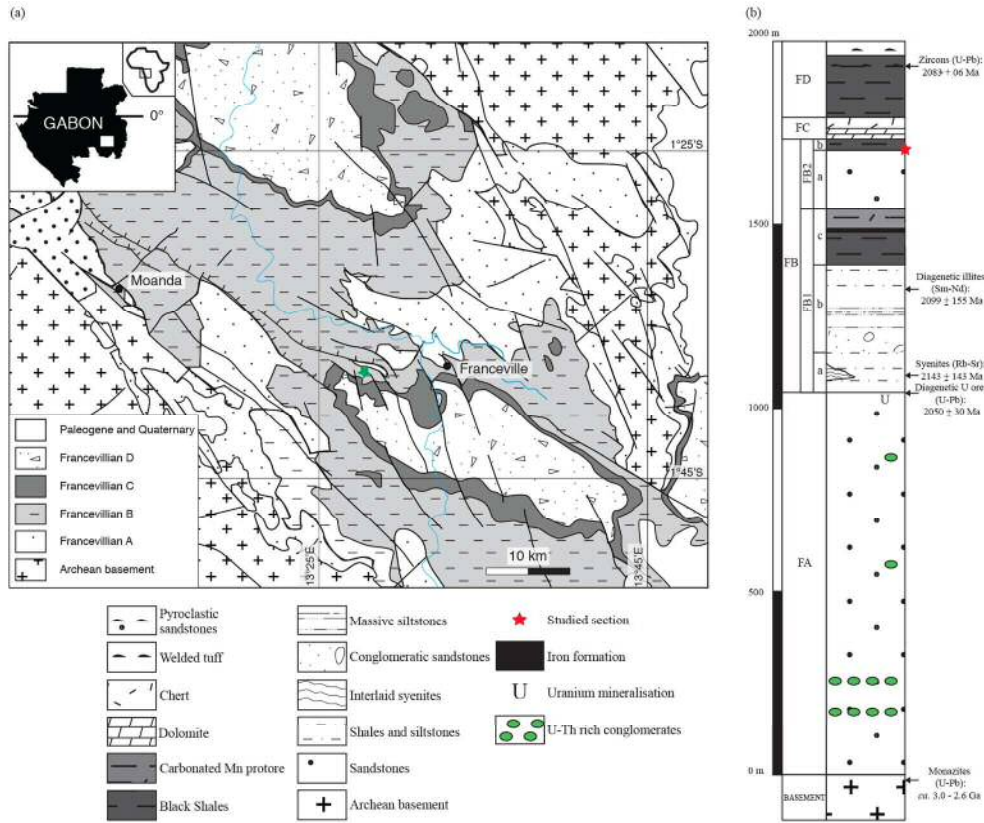


Figure 1

157x130mm (300 x 300 DPI)

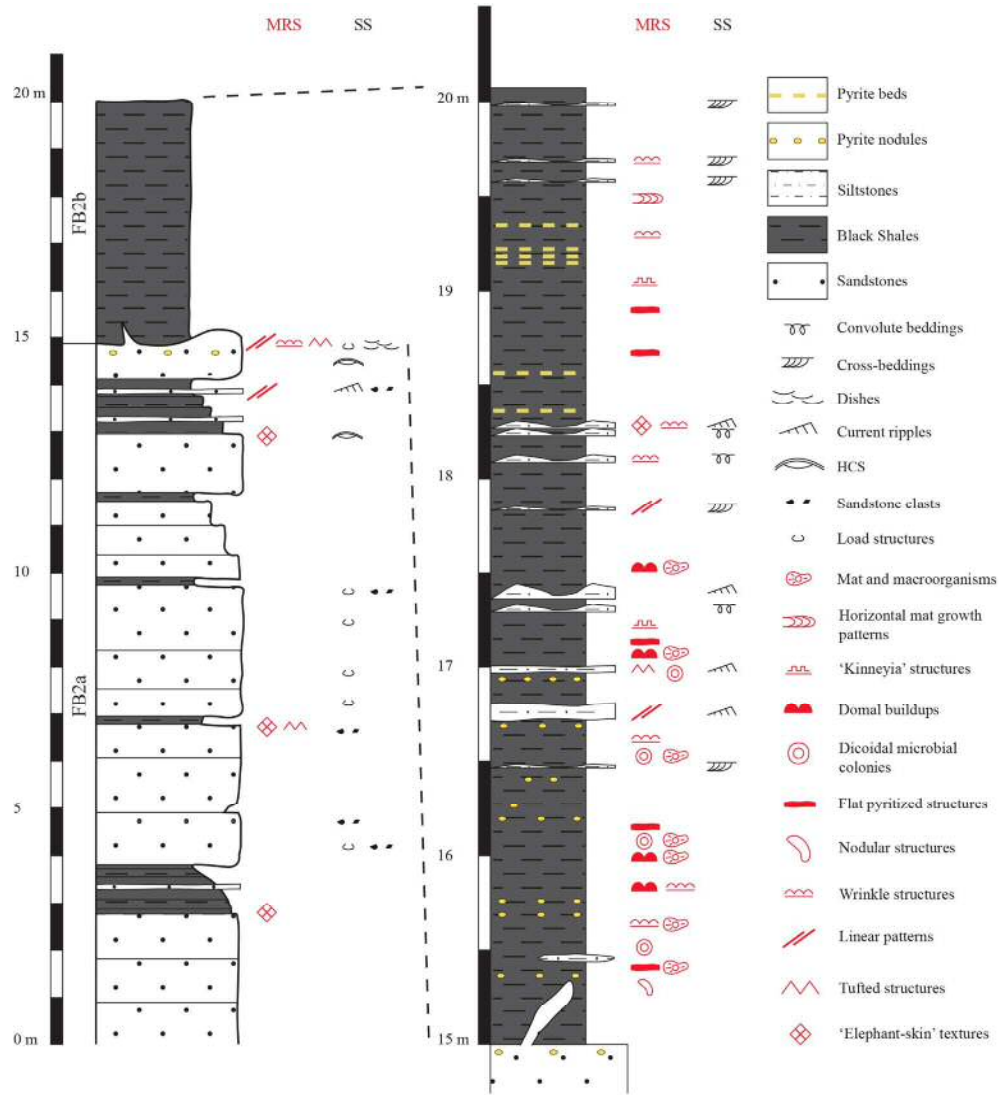


Figure 2

180x197mm (300 x 300 DPI)

1  
2  
3  
4  
5  
6  
7  
8  
9  
10  
11  
12  
13  
14  
15  
16  
17  
18  
19  
20  
21  
22  
23  
24  
25  
26  
27  
28  
29  
30  
31  
32  
33  
34  
35  
36  
37  
38  
39  
40  
41  
42  
43  
44  
45  
46  
47  
48  
49  
50  
51  
52  
53  
54  
55  
56  
57  
58  
59  
60

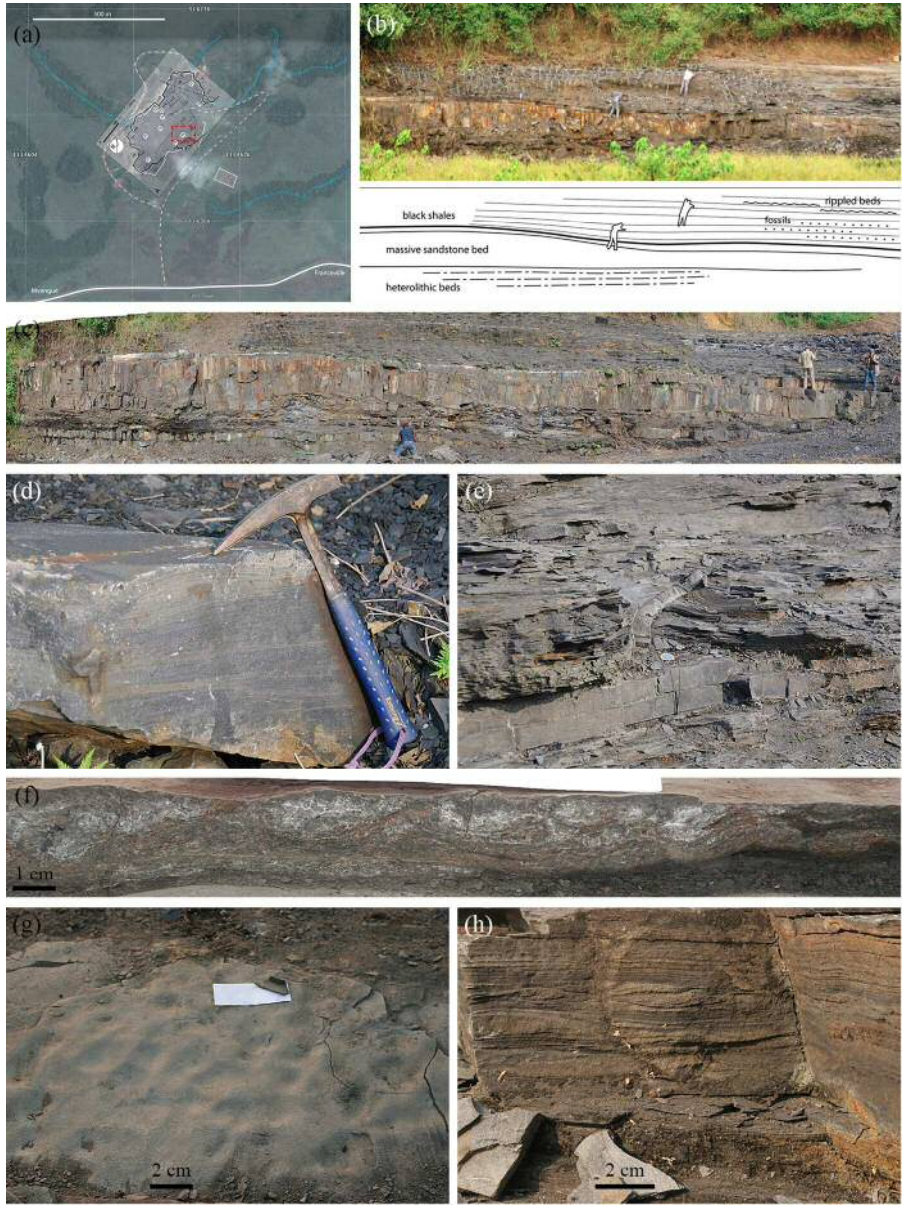


Figure 3

127x170mm (300 x 300 DPI)

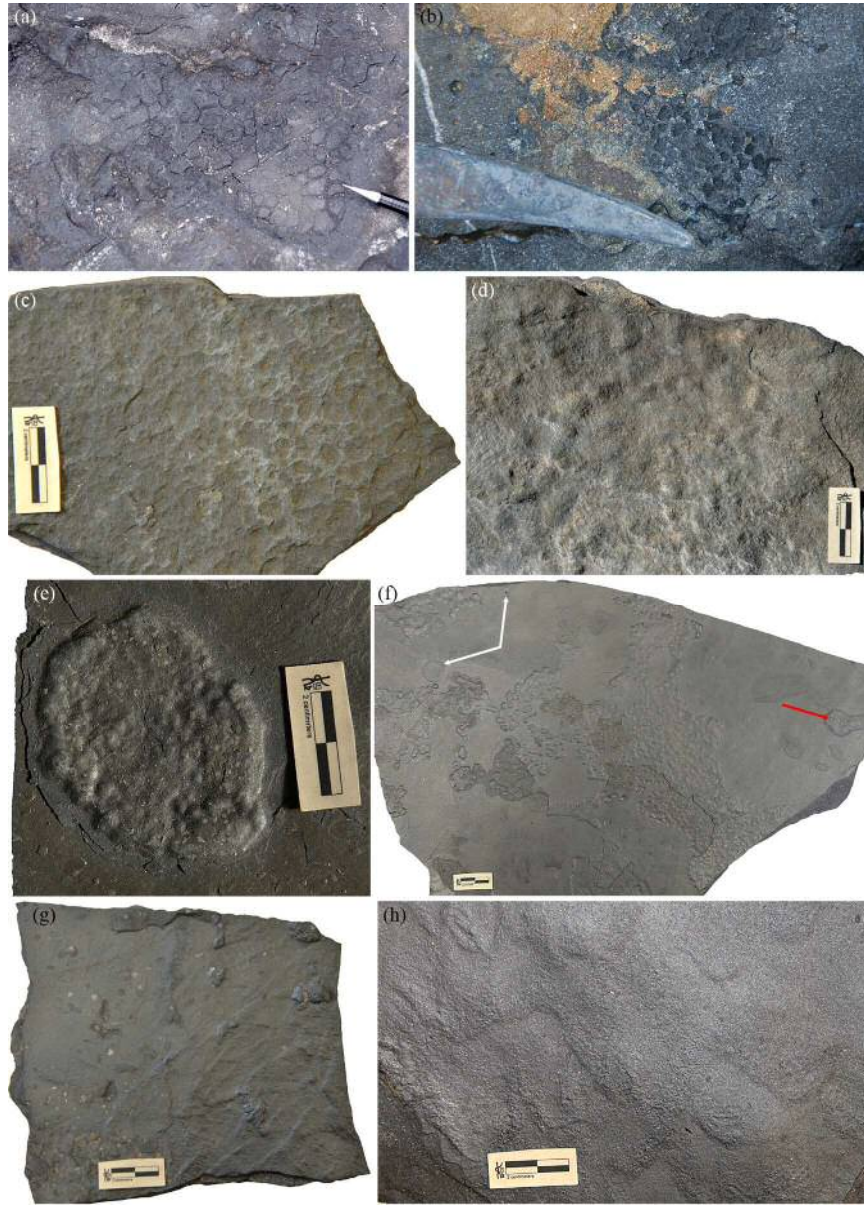


Figure 4

151x211mm (300 x 300 DPI)

1  
2  
3  
4  
5  
6  
7  
8  
9  
10  
11  
12  
13  
14  
15  
16  
17  
18  
19  
20  
21  
22  
23  
24  
25  
26  
27  
28  
29  
30  
31  
32  
33  
34  
35  
36  
37  
38  
39  
40  
41  
42  
43  
44  
45  
46  
47  
48  
49  
50  
51  
52  
53  
54  
55  
56  
57  
58  
59  
60

1  
2  
3  
4  
5  
6  
7  
8  
9  
10  
11  
12  
13  
14  
15  
16  
17  
18  
19  
20  
21  
22  
23  
24  
25  
26  
27  
28  
29  
30  
31  
32  
33  
34  
35  
36  
37  
38  
39  
40  
41  
42  
43  
44  
45  
46  
47  
48  
49  
50  
51  
52  
53  
54  
55  
56  
57  
58  
59  
60

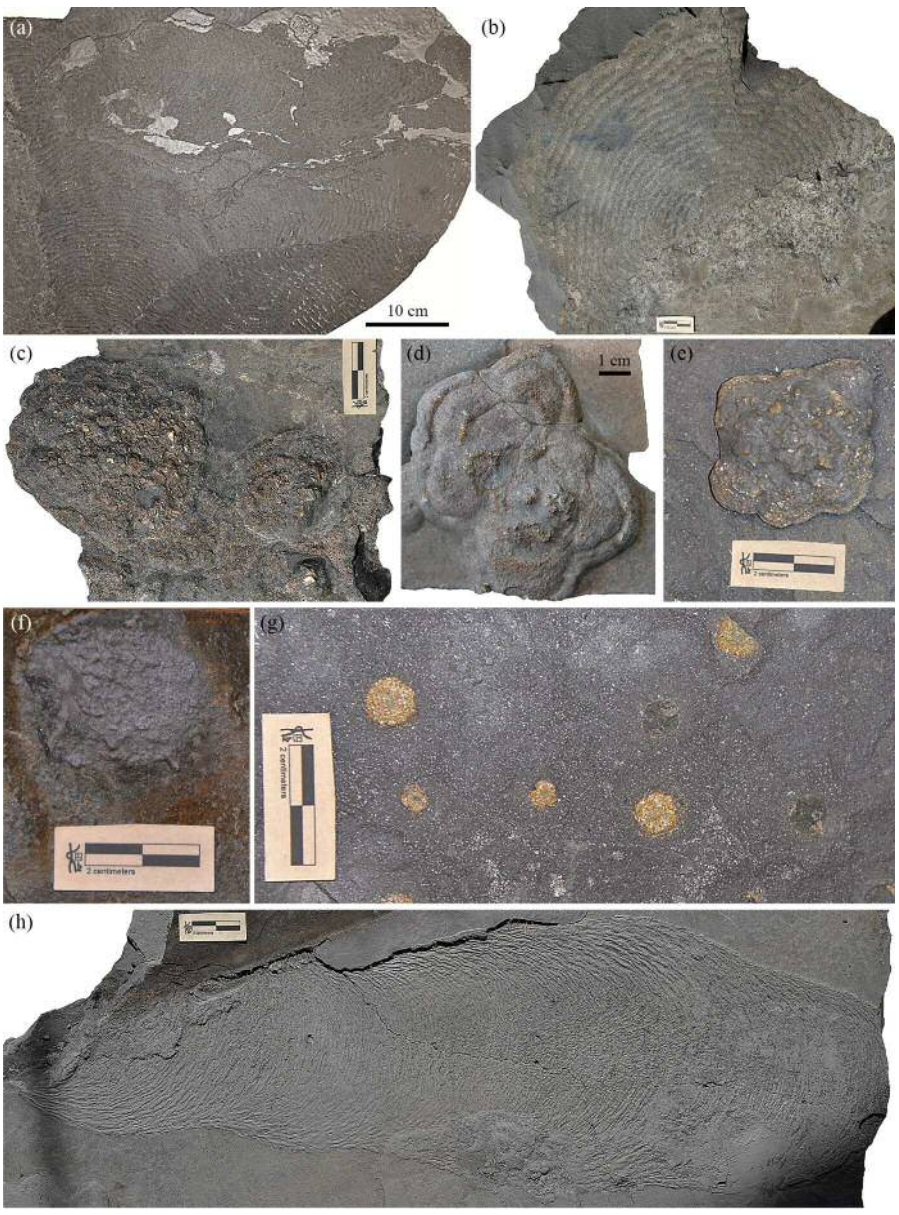


Figure 5

149x201mm (300 x 300 DPI)





Figure 6

142x185mm (300 x 300 DPI)

1  
2  
3  
4  
5  
6  
7  
8  
9  
10  
11  
12  
13  
14  
15  
16  
17  
18  
19  
20  
21  
22  
23  
24  
25  
26  
27  
28  
29  
30  
31  
32  
33  
34  
35  
36  
37  
38  
39  
40  
41  
42  
43  
44  
45  
46  
47  
48  
49  
50  
51  
52  
53  
54  
55  
56  
57  
58  
59  
60

1  
2  
3  
4  
5  
6  
7  
8  
9  
10  
11  
12  
13  
14  
15  
16  
17  
18  
19  
20  
21  
22  
23  
24  
25  
26  
27  
28  
29  
30  
31  
32  
33  
34  
35  
36  
37  
38  
39  
40  
41  
42  
43  
44  
45  
46  
47  
48  
49  
50  
51  
52  
53  
54  
55  
56  
57  
58  
59  
60

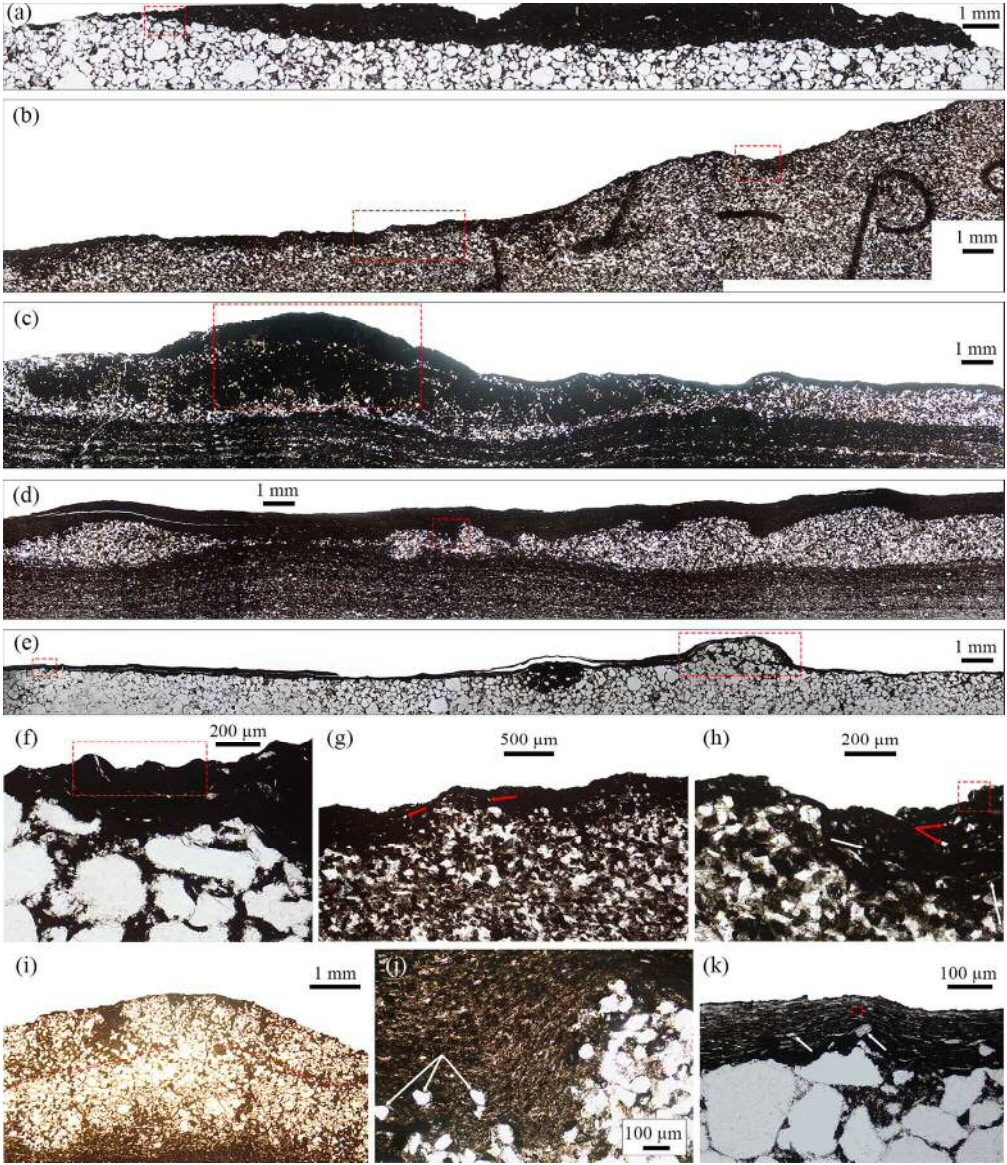


Figure 7

152x176mm (300 x 300 DPI)

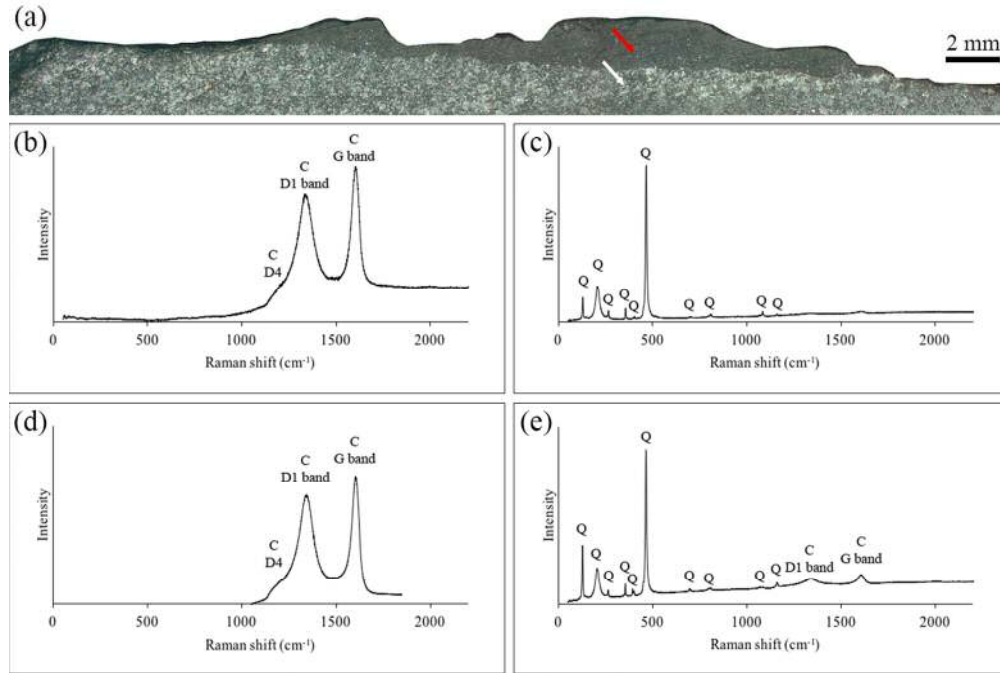


Figure 8

121x81mm (300 x 300 DPI)

View Only

1  
2  
3  
4  
5  
6  
7  
8  
9  
10  
11  
12  
13  
14  
15  
16  
17  
18  
19  
20  
21  
22  
23  
24  
25  
26  
27  
28  
29  
30  
31  
32  
33  
34  
35  
36  
37  
38  
39  
40  
41  
42  
43  
44  
45  
46  
47  
48  
49  
50  
51  
52  
53  
54  
55  
56  
57  
58  
59  
60

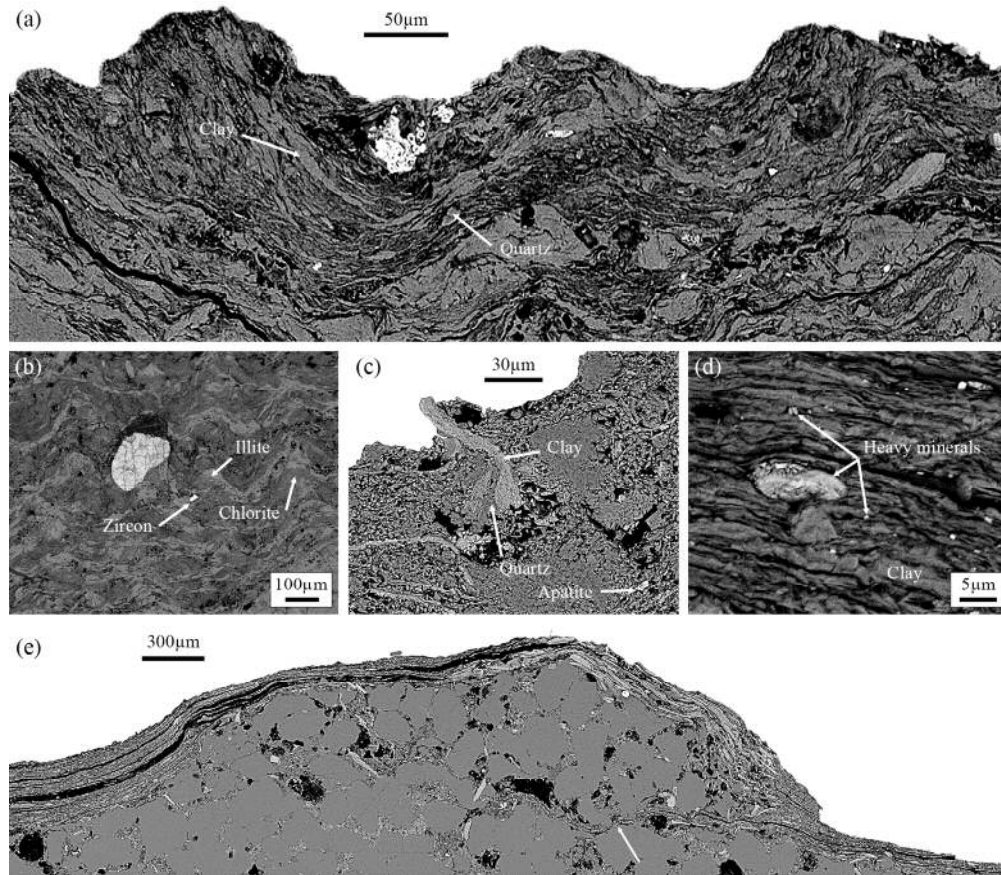


Figure 9

151x132mm (300 x 300 DPI)



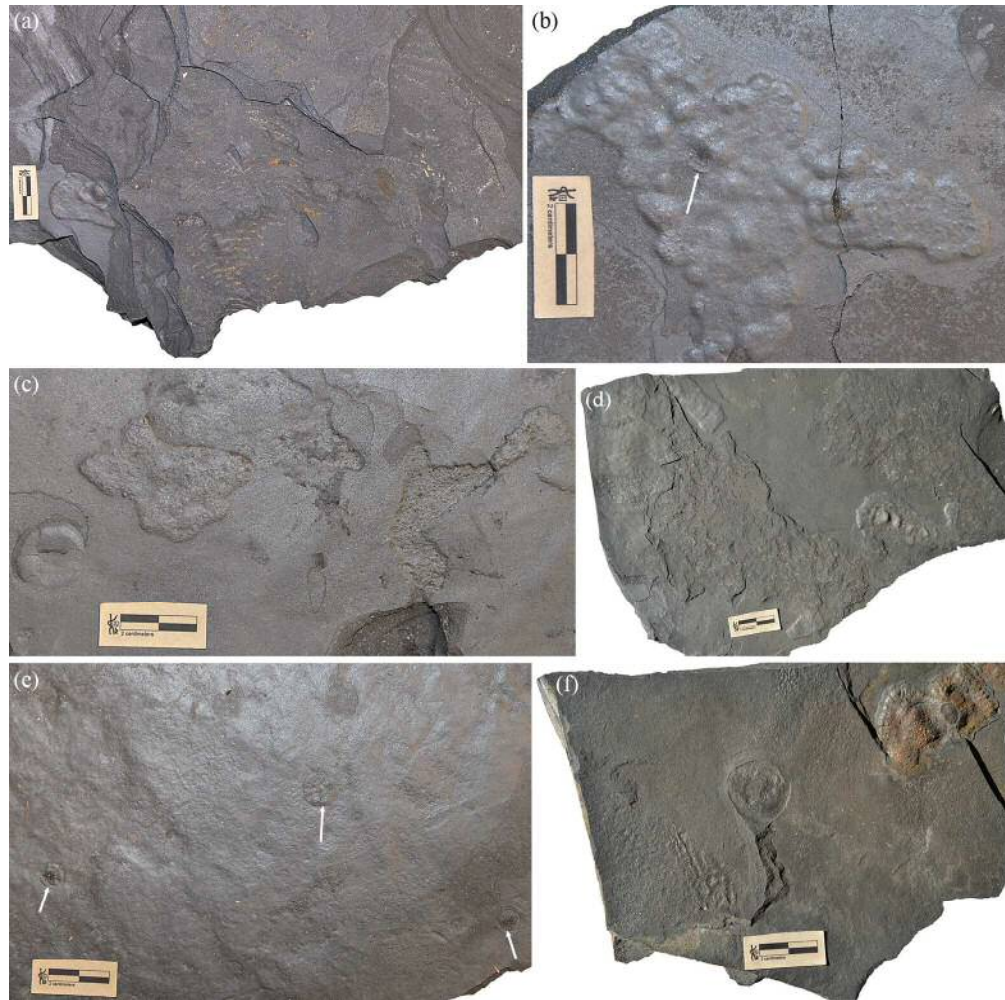


Figure 10

152x151mm (300 x 300 DPI)

1  
2  
3  
4  
5  
6  
7  
8  
9  
10  
11  
12  
13  
14  
15  
16  
17  
18  
19  
20  
21  
22  
23  
24  
25  
26  
27  
28  
29  
30  
31  
32  
33  
34  
35  
36  
37  
38  
39  
40  
41  
42  
43  
44  
45  
46  
47  
48  
49  
50  
51  
52  
53  
54  
55  
56  
57  
58  
59  
60

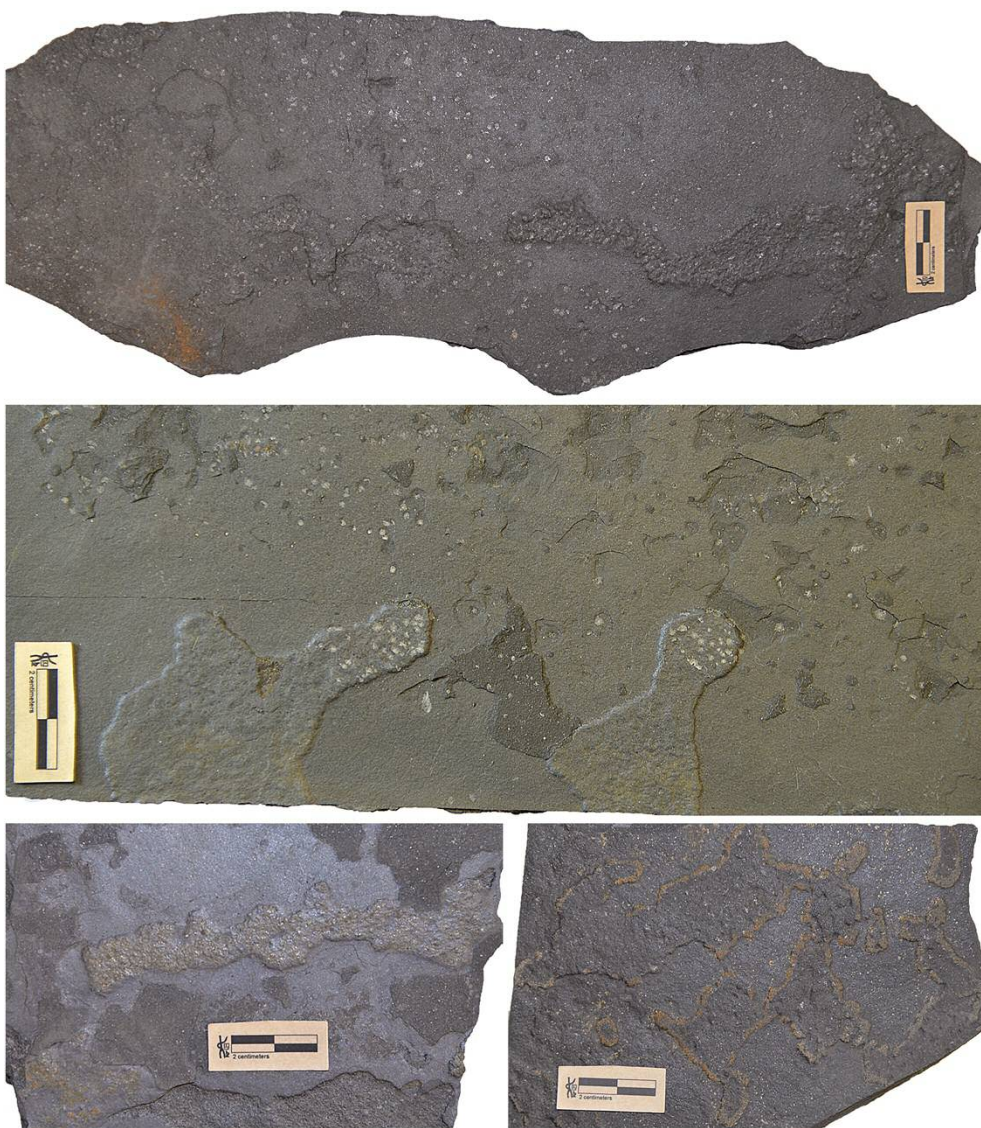
**TABLE 1  $\delta^{13}\text{C}$  values of organic matter in mat-related structures (MRS).**

Subunits	Samples	$\delta^{13}\text{C}_{\text{org}}$ (‰)
FB2b Black shale	MRS_1	-34.92
	MRS_2	-34.41
	MRS_3	-32.45
	MRS_4	-41.26
FB2a Sandstone	MRS_5	-31.68
	MRS_6-1	-32.72
	MRS_6-2	-33.32
	MRS_7	-33.95
	MRS_8	-33.55
	MRS_9	-33.66
	MRS_10	-33.61
	MRS_11	-32.28
	MRS_12	-30.67
	MRS_13	-31.95
MRS_14	-32.03	

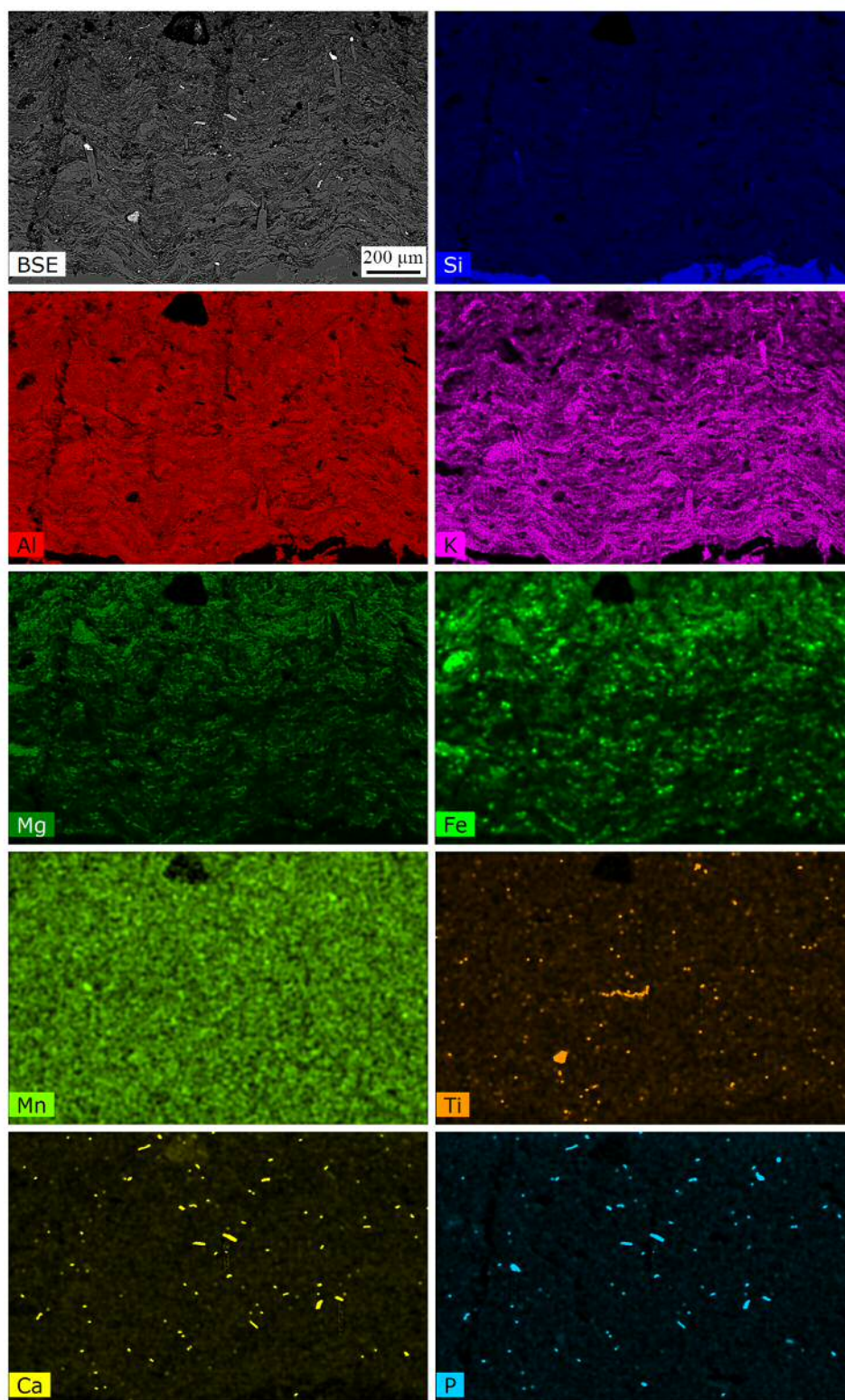
For Review Only

1  
2  
3 **1 Supplementary information**  
4

5  
6 **2**  
7 **3 FIGURE S1**  
8  
9



46 **30 FIGURE S1 Additional flat pyritized microbial mats.**  
47  
48  
49  
50  
51  
52  
53  
54  
55  
56  
57  
58  
59  
60

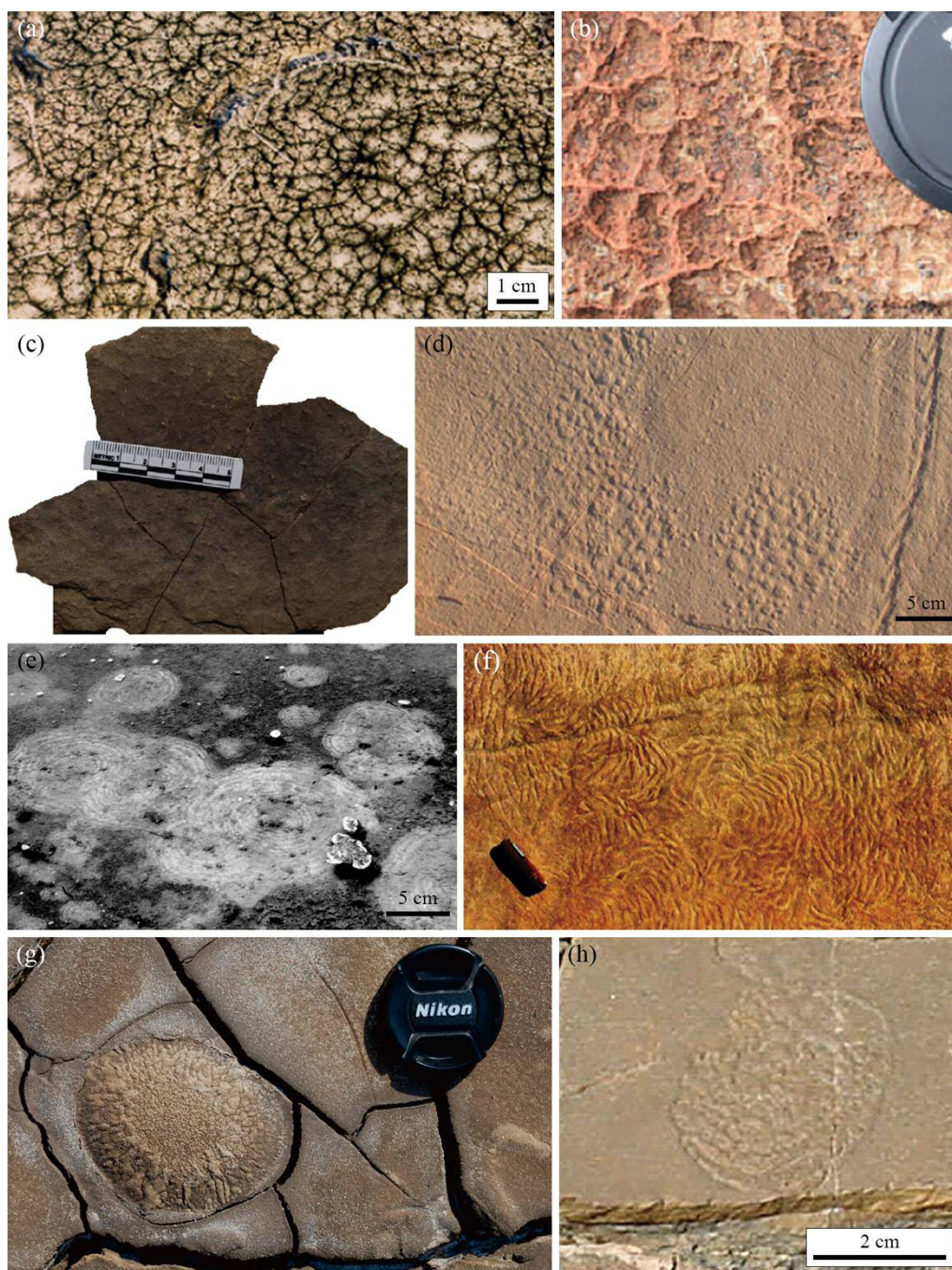
32 **FIGURE S2**

68 **FIGURE S2 EDS elemental maps of bulges of reticulate patterns in cross-section**  
 69 **perpendicular to bedding plane.** BSE and composite elemental maps. Note the wavy-crinkly  
 70 laminae with a large amount of embedded heavy minerals.

71



1  
2  
3 72 **FIGURE S3**  
4  
5 73  
6 74  
7 75  
8 76  
9 77  
10 78  
11 79  
12 80  
13 81  
14 82  
15 83  
16 84  
17 85  
18 86  
19 87  
20 88  
21 89  
22 90  
23 91  
24 92  
25 93  
26 94  
27 95  
28 96  
29 97  
30 98  
31 99  
32 100  
33 101  
34 102  
35 103  
36 104  
37 105  
38 106  
39 107  
40 108  
41 109  
42 110



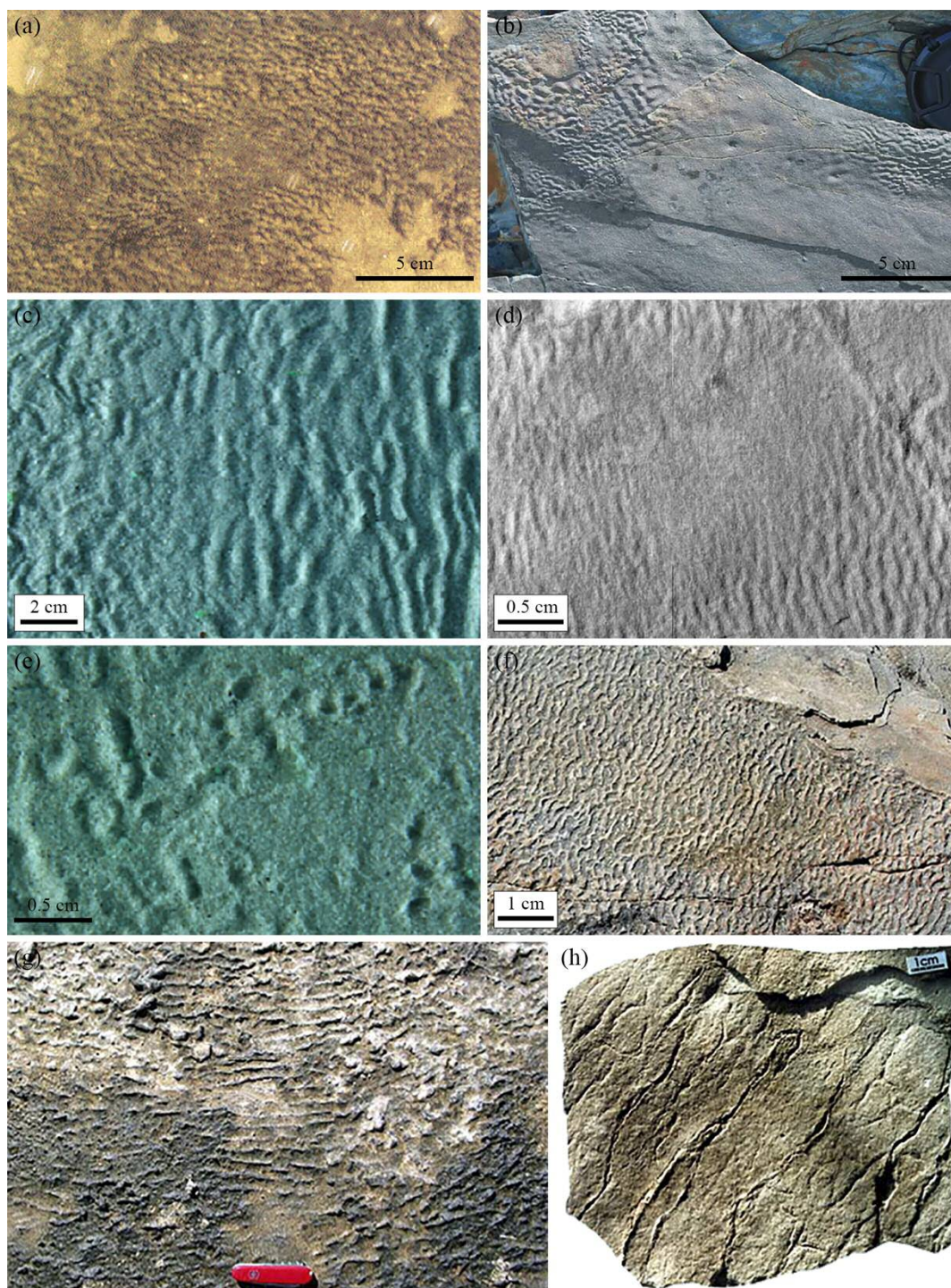
105 **FIGURE S3 Photographs of mat-layer structures found in literature.** (a) Analogous  
106 'elephant-skin' texture from modern lower supratidal, Bahar Alouane, southern Tunisia.  
107 Modified after photo published in Gerdes (2007). (b) Fossil reticulate pattern on bedding plane  
108 of siliciclastic beds from the Archean Tumbiana Formation, Australia. Modified after photo  
109 published in Flannery & Walter (2012). (c) A 2.0 billion-years-old tufted microbial mat from  
110 Makgabeng Formation, South Africa. Modified after photo published in Simpson *et al.* (2013).

1  
2  
3 111 (d) Analogue clustered low mound-like structures with *Protichnites* trackways on bedding  
4 112 surface of quartz arenites from the Late Cambrian, Elk Mound Group, USA. Modified after  
5 113 photo published in Bottjer & Hagadorn (2007). (e) Modern analogous 'fairy rings' on soft  
6 114 muddy sediments from Bretagne salterns, France. Modified after photo published in  
7 115 Grazhdankin & Gerdes (2007). (f) Ancient example of outward-convex, spindle-shaped  
8 116 discoidal structures with concentric rings from the Mesoproterozoic, Sonia Sandstone, India.  
9 117 Modified after photo published in Sarkar *et al.* (2014). (g) Modern discoidal microbial colony  
10 118 on tidal flat from the Gulf of Cambay, India. Modified after photo published in Banerjee *et al.*  
11 119 (2014). Lens cap diameter: 6 cm. (h) Analogue discoidal microbial colony on bedding plane of  
12 120 sandstones from the Precambrian Vindhyan Supergroup, India. Modified after photo published  
13 121 in Banerjee *et al.* (2014).  
14  
15  
16  
17  
18  
19  
20  
21  
22  
23  
24  
25  
26  
27  
28  
29  
30  
31  
32  
33  
34  
35  
36  
37  
38  
39  
40  
41  
42  
43  
44  
45  
46  
47  
48  
49  
50  
51  
52  
53  
54  
55  
56  
57  
58  
59  
60

For Review Only

123 **FIGURE S4**

124



156

157 **FIGURE S4 Photographs of mat-related structures found in literature.** (a) Modern  
 158 example of submerged wrinkle marks from Redfish Bay, Texas. Modified after photo published  
 159 in Hagadorn & Bottjer (1997). (b) Patches of wrinkle marks on bedding surface of fine-grained  
 160 sandstones from the Early Cambrian, Chapel Island Formation, Canada. Modified after photo  
 161 published in Buatois *et al.* (2014). (c) Parallel wavy wrinkle structures reproduced in wave tank

1  
2  
3 162 experiments using microbial aggregates. Modified after photo published in Mariotti *et al.*  
4  
5 163 (2014). (d) Analogous parallel wavy wrinkle structures on bedding plane of mudstones from  
6  
7 164 the Early Cambrian, Northwest Argentina. Modified after photo published in Buatois &  
8  
9 165 Mángano (2003). (e) Minute “Kinneyia” structures formed with microbial aggregates in wave  
10  
11 166 tank experiments. Modified after photo published in Mariotti *et al.* (2014). (f) Ancient analogue  
12  
13 167 “Kinneyia” structures on bedding surface of siltstones from the Cambrian, Oeland, Sweden.  
14  
15 168 Modified after photo published in Porada & Bouougri (2007). (g) Linear features from modern  
16  
17 169 tidal flats of Bhar Alouane, southern Tunisia. Modified after photo published in Porada &  
18  
19 170 Bouougri (2007). (h) Putative linear patterns on bedding surface of fine-grained quartzites from  
20  
21 171 the Neoproterozoic Katanga Supergroup, Zambia. Modified after photo published in Porada &  
22  
23 172 Bouougri (2007).

173

174

For Review Only

175 **TABLE S1**

176

Samples	Si	Al <sup>IV</sup>	Al <sup>VI</sup>	Al <sub>Tot</sub>	Mg	Fe	Ti	Mn	K	Na	Ca	Σ Oct	Int
EST	2.78	1.22	1.58	2.8	0.73	0.11	0	0	0.33	0.13	0	2.42	0.47
	3.13	0.87	1.69	2.56	0.15	0.12	0.02	0	0.71	0.15	0	1.98	0.86
	2.89	1.11	1.47	2.58	0.33	0.05	0	0	0.47	0.18	0	1.84	0.65
	3.13	0.87	1.91	2.78	0.11	0	0	0	0.74	0.1	0	2.02	0.84
	2.88	1.12	1.6	2.72	0.52	0.17	0	0	0.52	0.11	0	2.29	0.63
	3.11	0.89	1.94	2.83	0.09	0	0	0	0.79	0.1	0	2.03	0.89
	2.63	1.37	1.17	2.54	0.72	0	0.26	0	0.26	0.17	0	2.15	0.43
PTMM	3.54	0.46	1.79	2.25	0.06	0.04	0	0	0.65	0.06	0	1.89	0.71
	3.41	0.59	1.88	2.47	0.1	0	0	0	0.69	0.07	0	1.98	0.76
	3.34	0.66	1.76	2.41	0.15	0.04	0	0	0.71	0.09	0.03	1.95	0.87
	3.46	0.54	1.69	2.23	0.28	0.06	0	0	0.55	0.09	0	2.02	0.64
	3.61	0.39	1.8	2.19	0.14	0	0	0	0.47	0.17	0	1.94	0.64
	3.35	0.65	1.6	2.25	0.3	0.09	0.01	0.02	0.58	0.12	0.03	2.02	0.73
	3.16	0.84	1.77	2.61	0.14	0.04	0.02	0.02	0.48	0.29	0.04	1.98	0.8
	3.06	0.94	1.56	2.5	0.16	0.25	0.02	0.01	0.86	0.07	0.01	2	0.94
	2.98	1.02	1.83	2.85	0.08	0.04	0.01	0.01	0.89	0.03	0.04	1.98	0.95
	3.03	0.97	1.79	2.76	0.12	0.04	0.01	0.02	0.75	0.11	0.04	1.98	0.9
3.1	0.9	1.83	2.72	0.1	0.04	0.02	0.02	0.39	0.35	0.03	2	0.77	
PWWS	3.17	0.83	1.39	2.22	0.46	0.4	0	0	0.41	0.12	0	2.25	0.53
	3.44	0.56	1.66	2.21	0.3	0.13	0	0	0.45	0.14	0	2.09	0.59
	3.56	0.44	1.67	2.11	0.24	0.1	0	0	0.53	0.09	0	2.02	0.62
	3.38	0.62	1.27	1.89	0.53	0.4	0.03	0	0.34	0.09	0	2.23	0.43
	3.17	0.83	1.91	2.75	0.12	0	0	0	0.75	0.1	0	2.03	0.85
	3.82	0.18	1.77	1.94	0.15	0	0	0	0.5	0.08	0	1.92	0.57
	3.1	0.9	1.76	2.66	0.18	0.07	0.01	0.02	0.62	0.14	0.02	2.03	0.78
	3.04	0.96	1.5	2.46	0.17	0.23	0.07	0.02	0.79	0.09	0.02	1.99	0.89
	3.18	0.82	1.62	2.44	0.32	0.15	0.01	0.02	0.47	0.18	0.02	2.12	0.68
	3.07	0.93	1.39	2.32	0.48	0.3	0.02	0.03	0.55	0.08	0.01	2.22	0.65
2.97	1.03	1.39	2.42	0.47	0.31	0.04	0.03	0.53	0.13	0.02	2.24	0.67	
LP	3.19	0.81	1.85	2.66	2.38	1.64	0.12	0	0.1	0.18	0	5.99	0.28
	3.31	0.69	2.12	2.81	2.48	1.98	0	0	0.02	0.06	0	6.57	0.08
	3.41	0.59	2.25	2.83	2.37	1.64	0.12	0	0.15	0.07	0	6.37	0.22
	3.06	0.94	2.48	3.42	1.98	2.07	0	0	0.2	0.08	0	6.53	0.28
	2.95	1.05	1.5	2.56	0.41	0.29	0.03	0	0.65	0.09	0	2.23	0.74
	3.08	0.92	1.88	2.8	0.08	0.06	0	0	0.77	0.18	0	2.02	0.95
	3.19	0.81	1.82	2.62	0.1	0.06	0	0	0.86	0.05	0	1.98	0.91
	3.11	0.89	0.99	1.88	0.43	0.54	0.09	0.05	0.44	0.05	0.06	2.1	0.55
3.72	0.28	1.44	1.72	0.12	0.1	0.11	0.03	0.48	0.12	0.03	1.8	0.63	

177

1  
2  
3 178 **TABLE S1 Representative structural formulae of clays from microbial mats studied with**  
4  
5 179 **EDS.** EST, ‘elephant-skin’ texture; PTMM, putative tufted microbial mat; WS, wrinkle  
6  
7 180 structure; LP, linear pattern.

8 181

9 182

10 183

11  
12  
13 184 **TABLE S2**

14 185

Samples	Mass (mg)	%C	%S
EST_mat	10.63	8.62	0.25
EST_host rock	16.62	0.58	0.05
DB_mat	15.32	0.53	22.16
DB_host rock	13.24	4.59	0.22
PWWS_mat	10.37	1.69	0.00
PWWS_host rock	14.17	2.2	0.00
sample4_mat	16.08	1.86	0.06
sample4_host rock	17.53	1.77	0.09
sample5_mat	12.58	1.25	0.54
sample5_host rock	13.18	2.11	0.11

15  
16  
17  
18  
19  
20  
21  
22  
23  
24  
25  
26  
27  
28  
29  
30  
31  
32  
33  
34 186

35  
36 187 **TABLE S2 Organic elemental analyses (carbon and sulfur) on five microbial mats and**  
37  
38 188 **their host sediments from the FB2 Formation.** EST, ‘elephant-skin’ texture; DB, domal  
39  
40 189 buildup; PWWS, parallel wavy wrinkle structure.